



Studienarbeit / 2025

# Aerodynamic Design of a Fowler Flap for a Hybrid Laminar Flow Control Airfoil

by:

Shrinidhi Holenarsipura Murali Madhava  
(Matrikelnummer 5304013)

supervised by:

Prof. Dr.-Ing. Ingo Staack  
Dr.-Ing. Stanislav Karpuk

April 2025

Institute of Aircraft Design and Lightweight Structures (IFL)  
Technische Universität Braunschweig



## Studienarbeit

für Herrn Shrinidhi Holenarsipura Murali Madhava

Matr. Nr. 5304013

### Aerodynamic Design of a Fowler Flap for a Hybrid Laminar Flow Control Airfoil

Issued: 12 December, 2024

Submitted: 06 January, 2025

#### Introduction

The need for sustainable and energy-efficient air transport pushes the aviation industries toward the design of next-generation aircraft, with dramatic energy consumption, emission, and noise. The Cluster of Excellence SE2A – Sustainable and Energy Efficient Aviation is an interdisciplinary research center investigating technologies for sustainable and energy-efficient air transport systems. One of the important streams of technology assessments is related to the overall aircraft design and investigations of unconventional aircraft configurations with future technologies.

The present project is focused on the design of a Fowler Flap for an airfoil applied to the airfoil featuring hybrid laminar flow control (HLFC) technology.

#### Tasks

- Define and modify an existing design methodology for a rapid CFD analysis of airfoils.
- Perform parametric studies of a Fowler flap.
- Obtain a new design and compare key aerodynamic characteristics between the original and the final configurations.

Dr.-Ing S. Karpuk

## Declaration of copyright

I hereby declare that I have written the Studienarbeit ‘Aerodynamic Design of a Fowler Flap for a Hybrid Laminar Flow Control Airfoil’ independently and without unauthorized outside help and only with the permissible aids previously announced by the teaching staff and that I have not yet submitted this thesis for this or any other examination. I have fully indicated all sources and aids used.

I am aware that attempts at cheating - in particular proven plagiarism as well as incomplete information on sources and aids - can lead to the final failure of an examination and thus to failure of the whole course of study according to §11, cl. 4 of the General Examination Regulations.

30.04.2025

Date

Shrinidhi. K.M

Signature

## Abstract

The aerodynamic performance of high-lift devices is crucial for aircraft operation, particularly during low-speed flight phases of takeoff and landing. This research focuses on maximizing the lift coefficient ( $C_L$ ) of a Fowler flap applied to a Hybrid Laminar Flow Control (HLFC) airfoil that incorporates a fixed drooping nose. The objective is to achieve maximized lift performance at fixed flap deflection angles of 15 degrees and 30 degrees, corresponding to takeoff and landing configurations respectively, while also evaluating the flap's aerodynamic behavior across a range of angles of attack relevant to these flight regimes.

To confirm the correctness of the numerical approach, a mesh sensitivity analysis was conducted between the baseline mesh, a finer mesh, and a coarser mesh. The computed maximum lift coefficient ( $C_{L_{\max}}$ ) for the baseline differed by only 0.27% from the fine mesh, indicating grid independence. Given this negligible deviation, the baseline mesh was chosen to balance computational cost and accuracy, which is essential for practical engineering applications.

The analysis was conducted using an automated simulation process consisting of Py-AeroSweep (Python-based Computational Fluid Dynamics (CFD) analysis framework), SU2 (open-source CFD solver), Fidelity Pointwise (mesh generation and manipulation), ParaView & MS Excel (post-processing). A systematic parameter sensitivity study was conducted to identify key design parameters influencing  $C_L$ . A sequential, One-At-A-Time (OAT) optimization approach was employed, refining individual parameters while holding previously optimized values constant. Critical design variables were iteratively adjusted based on their impact on  $C_L$ .

The final optimized flap design was compared against the baseline configuration and exhibited a significant improvement in lift performance (increase in  $C_{L_{\max}}$  by 4.14% for 15-degree flap deflection and 4.56% for 30-degree flap deflection).

This research provides valuable insights into the design optimization of a high-lift device for an HLFC airfoil and establishes a foundation for more sophisticated aerodynamic design methodologies in the future.

# Table of Contents

<b>Abstract</b>	<b>I</b>
<b>Table of Contents</b>	<b>II</b>
<b>List of Figures</b>	<b>III</b>
<b>List of Tables</b>	<b>V</b>
<b>List of Symbols</b>	<b>VI</b>
<b>1 Introduction</b>	<b>1</b>
1.1 Motivation . . . . .	1
1.2 State of the art . . . . .	2
1.3 Approach . . . . .	5
<b>2 Methodology</b>	<b>7</b>
2.1 PyAeroSweep . . . . .	7
2.1.1 Framework prerequisites . . . . .	7
2.1.2 Workflow description . . . . .	9
2.1.3 Geometry definition . . . . .	12
2.1.4 Mesh generation . . . . .	12
2.1.5 Numerical solver and simulation setup . . . . .	16
2.2 Concluding remarks . . . . .	18
<b>3 Trade Studies</b>	<b>19</b>
3.1 Fowler flap design optimization strategy . . . . .	19
3.1.1 Mesh sensitivity study . . . . .	20
3.1.2 Parameter sensitivity study . . . . .	23
3.2 Concluding remarks . . . . .	35
<b>4 Results</b>	<b>36</b>
4.1 Flap design parameters . . . . .	36
4.2 Aerodynamic performance at 15-degree flap deflection . . . . .	39
4.3 Aerodynamic performance at 30-degree flap deflection . . . . .	46
4.4 Limitations and future work . . . . .	54
4.5 Concluding remarks . . . . .	56
<b>5 Summary</b>	<b>57</b>
<b>Bibliography</b>	<b>58</b>
<b>Appendix</b>	<b>60</b>
A Input_data.py for the case Flapped_airfoil_full . . . . .	60
B Geometric input data for the HLFC airfoil: PARSEC & CST . . . . .	65
C SU2: Solver configuration file . . . . .	66

# List of Figures

1.1	Effect of high-lift devices on the lift coefficient ( $C_L$ ) and the angle of attack ( $\alpha$ ). Reproduced from [12]. . . . .	3
1.2	Mechanism of the fowler flap. Reproduced from [12], [18]. . . . .	5
2.1	PyAeroSweep: Framework. . . . .	8
2.2	PARSEC Airfoil. . . . .	9
2.3	PyAeroSweep - Flapped airfoil PARSEC folder. . . . .	11
2.4	Key flap geometry definitions. Reproduced from [21]. . . . .	13
2.5	(a) Horizontal overlap $x\_gap$ and (b) Vertical gap $y\_gap$ definitions. . . . .	13
2.6	Computational mesh around the HLFC airfoil. . . . .	15
2.7	Detailed view of the computational mesh around the Fowler flap. . . . .	15
3.1	Fowler flap design optimization strategy. . . . .	19
3.2	Impact of mesh refinement on maximum lift coefficient ( $C_{L_{max}}$ ). . . . .	21
3.3	Effect of mesh refinement on grid resolution. . . . .	22
3.4	Aerodynamic performance characteristics ( $C_L$ & $C_D$ ) as a function of angle of attack ( $\alpha$ ) for varying $x\_gap$ at a fixed $y\_gap$ of 4.0% of the airfoil chord. . . . .	27
3.5	Aerodynamic performance characteristics ( $C_L$ & $C_D$ ) as a function of angle of attack ( $\alpha$ ) for varying $y\_gap$ at a fixed $x\_gap$ of 4.3% of the airfoil chord. . . . .	28
3.6	Eddy viscosity contours: Comparison of baseline and optimized $x\_gap$ & $y\_gap$ configurations at 4-degree AoA and 30-degree flap deflection. . . . .	29
3.7	Eddy viscosity contours: Comparison of baseline and optimized $x\_gap$ & $y\_gap$ configurations at 13-degree AoA and 30-degree flap deflection. . . . .	30
3.8	Comparison of baseline and updated configuration: Aerodynamic performance characteristics ( $C_L$ & $C_D$ ) as a function of angle of attack ( $\alpha$ ) . . . . .	32
3.9	Eddy viscosity contours: Comparison of baseline and updated $x\_gap$ & $y\_gap$ configurations at 4-degree AoA and 30-degree flap deflection. . . . .	33
3.10	Eddy viscosity contours: Comparison of baseline and updated $x\_gap$ & $y\_gap$ configurations at 13-degree AoA and 30-degree flap deflection. . . . .	34
4.1	Comparison of baseline and optimized airfoil and flap geometric profiles (all parameters optimized). . . . .	38
4.2	Comparison of baseline and optimized aerodynamic performance for the 15-degree flap deflection configuration (all parameters optimized). . . . .	41
4.3	Turbulent kinetic energy contours: Comparison of baseline and optimized configurations at 4-degree AoA and 15-degree flap deflection. . . . .	42
4.4	Turbulent kinetic energy contours: Comparison of baseline and optimized configurations at 15-degree AoA and 15-degree flap deflection. . . . .	43
4.5	Eddy viscosity contours: Comparison of baseline and optimized configurations at 4-degree AoA and 15-degree flap deflection. . . . .	44
4.6	Eddy viscosity contours: Comparison of baseline and optimized configurations at 15-degree AoA and 15-degree flap deflection. . . . .	45
4.7	Comparison of baseline and optimized aerodynamic performance for the 30-degree flap deflection configuration (all parameters optimized) . . . . .	49
4.8	Turbulent kinetic energy contours: Comparison of baseline and optimized configurations at 4-degree AoA and 30-degree flap deflection. . . . .	50

4.9	Turbulent kinetic energy contours: Comparison of baseline and optimized configurations at 13-degree AoA and 30-degree flap deflection. . . . .	51
4.10	Eddy viscosity contours: Comparison of baseline and optimized configurations at 4-degree AoA and 30-degree flap deflection. . . . .	52
4.11	Eddy viscosity contours: Comparison of baseline and optimized configurations at 13-degree AoA and 30-degree flap deflection. . . . .	53
4.12	PyAeroSweep error: Terminal output. . . . .	54
4.13	Equiangle skewness distribution of the baseline computational mesh. . . . .	55

## List of Tables

2.1	Predefined test cases in PyAeroSweep.	7
2.2	Geometric parameters for the baseline flap design.	14
3.1	Results of the mesh sensitivity study.	20
3.2	Simulation freestream conditions and reference length (airfoil chord).	23
3.3	Range of geometric parameters for the to-be optimized flap design.	25
4.1	Baseline and optimized flap design parameters (in ratios).	37
5.1	Summary of maximum lift coefficient ( $C_{L_{\max}}$ ) improvements.	57

# List of Symbols

## Abbreviations

Abbreviation	Meaning
HLFC	Hybrid Laminar Flow Control
EU	European Union
NO <sub>X</sub>	Nitrogen Oxide
ICAO	International Civil Aviation Organization
CORSIA	Carbon Offsetting and Reduction Scheme for International Aviation
BLS	Boundary Layer Suction
MDO	Multidisciplinary Design Optimization
IFL	Institut für Flugzeugbau und Leichtbau
AFC	Active Flow Control
CFD	Computational Fluid Dynamics
HiFi	High Fidelity
FFD	Free Form Deformation
T-Rex	Turbulence-Resolving Extruder
ISA	International Standard Atmosphere
SA	Spalart-Allamaras
SST	Shear Stress Transport
RANS	Reynolds-Averaged Navier-Stokes
URANS	Unsteady Reynolds-Averaged Navier-Stokes
CST	Class Shape Transformation
PARSEC	PARAmetric Airfoil SHAPE Class
AoA	Angle of Attack
OAT	One-At-A-Time
TKE	Turbulent Kinetic Energy
SBO	Surrogate-Based Optimization
SE <sup>2</sup> A	Sustainable and Energy-Efficient Aviation

## Latin symbols

Symbol	Unit	Meaning
$C_L$	-	Coefficient of Lift
$C_D$	-	Coefficient of Drag
$C_f$	-	Coefficient of Friction
$C_M$	-	Coefficient of Momentum
$Y^+$	-	Dimensionless Wall Distance
$Re_x$	-	Reynolds Number
$U_\infty$	m/s	Free Stream Velocity
$Ma$	-	Mach Number
$U_{fric}$	m/s	Friction Velocity
$C$	m	Chord Length

## Greek symbols

Symbol	Unit	Meaning
$\alpha$	Deg	Angle of Attack
$k$	$\text{m}^2/\text{s}^2$	Turbulent Kinetic Energy
$\omega$	1/s	Specific Rate of Dissipation
$\epsilon$	$\text{m}^2/\text{s}^3$	Turbulent Kinetic Energy Dissipation Rate
$\rho$	$\text{kg}/\text{m}^3$	Density
$\mu$	$\text{kg}/\text{m.s}$	Dynamic Viscosity
$\tau_{wall}$	$\text{kg}/\text{m.s}^2$	Wall Shear Stress

## Indices

Symbol	Meaning
$( \ )_{max}$	Maximum value

# 1 Introduction

## 1.1 Motivation

The European Union has made a strong commitment to leading the way in sustainable aviation. Through its "EU Flightpath 2050" initiative, the EU has laid out a comprehensive plan for a more environmentally responsible and efficient air transport system. The goal is ambitious: to cut emissions per passenger-kilometer by up to 75% and reduce nitrogen oxide ( $\text{NO}_x$ ) emissions by 90% [1]. This reflects the EU's recognition of the urgent need to tackle aviation's environmental impact and pave the way for a more sustainable future for air travel.

However, it is not just the EU that is focusing on sustainability. The global aviation industry, too, is taking action. The International Civil Aviation Organization (ICAO), a United Nations agency, has implemented programs such as the Carbon Offsetting and Reduction Scheme for International Aviation (CORSIA) aimed at reducing  $\text{CO}_2$  emissions from international flights [2]. At the same time, leading aircraft manufacturers like Airbus and Boeing are setting their own sustainability goals. These include developing fuel-efficient planes, exploring alternative fuels, and improving operational efficiency through advanced aerodynamic technologies like winglets [3], laminar flow control [4], and others. For instance, Airbus is working on zero-emission concept aircrafts [5].

To achieve these ambitious sustainability goals, aviation needs continuous innovation. Breakthroughs in aircraft design, engine technology, and sustainable fuels are key to cutting emissions and reducing noise. Advancements such as winglets help reduce fuel consumption and  $\text{CO}_2$  emissions by up to 4-5% and newer turbofan engines can improve fuel efficiency by as much as 15% compared to older designs. The A350, for instance, has a 40% smaller noise footprint than previous-generation aircraft. Furthermore, laminar flow technology can significantly reduce drag and energy consumption, which in turn lowers emissions [6].

A key aspect of achieving sustainability goals in aviation is optimizing aerodynamic performance during critical flight phases, particularly during take-off and landing. This study on aerodynamic flap optimization specifically targets the design of the Fowler flap, which plays a crucial role in improving lift generation and overall aircraft efficiency. High-lift devices, such as Fowler and Krueger flaps, significantly increase the maximum lift coefficient—up to 100% [7]. This directly impacts take-off and landing performance, where effective lift generation is essential. By optimizing flap designs, this study aims to maximize lift generation and improve aerodynamic efficiency, ultimately contributing to reducing fuel consumption and emissions, especially during low-speed, high-lift operations.

In addition to optimizing the flap design itself, the airfoil on which it is mounted incorporates advanced technologies such as Hybrid Laminar Flow Control (HLFC), which further enhance aerodynamic performance. Technologies like Boundary-Layer Suction (BLS) and HLFC have been shown to reduce drag and optimize overall aerodynamic

efficiency. The integration of these technologies within a Multidisciplinary Design Optimization (MDO) framework has been explored [8]. Building on these advancements, this study narrows its focus specifically to the optimization of the Fowler flap, refining its parameters to improve lift characteristics and overall performance during critical flight phases.

This study focuses on the aerodynamic optimization of a Fowler flap on a Hybrid Laminar Flow Control (HLFC) airfoil. While the airfoil already incorporates HLFC technologies, the research concentrates solely on refining the flap design. The study adapts the framework developed by Dr.-Ing. Stanislav Karpuk at the Institut für Flugzeugbau und Leichtbau (IFL) for Computational Fluid Dynamics (CFD) simulations. The research includes performing mesh and parameter sensitivity studies, comparing the baseline Fowler flap design with an optimized version, and evaluating potential aerodynamic performance improvements, particularly during take-off and landing phases.

### 1.2 State of the art

The aircraft wings are primarily optimized for cruise conditions, where aerodynamic efficiency is a key design driver [9]. However, during take-off and landing, the wing must generate sufficient lift at significantly lower speeds to ensure safe and efficient operation [10]. The lift coefficient ( $C_L$ ) required in these phases is much higher than in cruise, as the dynamic pressure at lower speeds is reduced[11]. Without additional lift augmentation, aircraft would require excessively long runways to reach the necessary takeoff speed or would face unsafe approach speeds during landing.[12]

To address this, high-lift systems are implemented to enhance the aerodynamic performance of the wing at low speeds. These systems typically include leading-edge and trailing-edge devices that modify the airfoil's camber and, in some cases, introduce controlled flow separation to increase lift [13][14][15]. The primary objective is to maximize the lift coefficient ( $C_{L_{max}}$ ) while maintaining acceptable drag and ensuring stable flow characteristics [16].

Early aircraft utilized simple high-lift devices like fixed leading-edge slats and plain flaps. These devices, while rudimentary, significantly improved take-off and landing performance by increasing the wing's camber and delaying stall [9]. Whereas, the modern aircraft design emphasizes integrated high-lift systems, combining leading-edge slats and trailing-edge flaps with sophisticated control systems. The Airbus A350, for example, utilizes optimized Fowler flap systems and slats, designed to reduce weight and complexity compared to earlier designs [17] [18].

The effects of leading and trailing-edge devices on the lift coefficient ( $C_L$ ) and the Angle of Attack ( $\alpha$ ) are illustrated in Figure 1.1. A leading-edge device primarily extends the lift curve by increasing the range of angles of attack over which the wing can linearly generate lift. This results in the lift coefficient being pushed to higher angles of attack, allowing the airfoil to achieve a higher maximum lift coefficient ( $C_{L_{max}}$ ) before flow separation leads to stall. However, during the lower angles of attack, where the wing operates

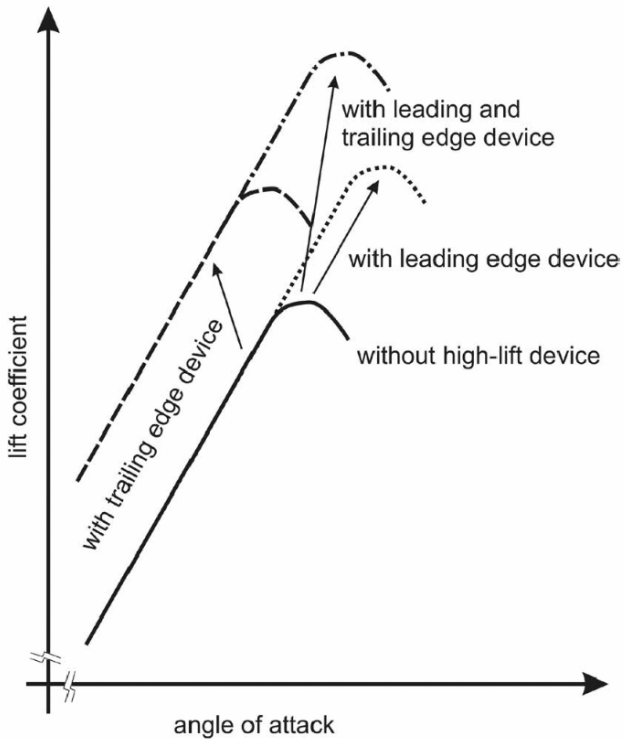


**Figure 1.1:** Effect of high-lift devices on the lift coefficient ( $C_L$ ) and the angle of attack ( $\alpha$ ). Reproduced from [12].

in the linear range, the leading-edge device has minimal impact on the lift coefficient. This device is most effective at delaying the onset of stall, enabling the wing to operate at higher angles of attack without a loss in lift, thereby increasing the wing's stall margin [12].

In contrast, a trailing-edge device generates a more consistent and significant increase in the lift coefficient throughout the entire range of angles of attack. The deflection of the trailing edge alters the Kutta condition, which, in turn, increases the wing's camber and effective incidence. Consequently, the airfoil generates more lift for a given angle of attack, and the onset of flow separation (stall) is delayed. The lift coefficient of an airfoil equipped with a trailing-edge device can be approximated within the linear range by accounting for both the angle of attack and the flap deflection. The increase in lift is typically proportional to the flap deflection, though the exact lift coefficient will depend on the angle of attack and the amount of trailing edge deflection [12].

When both leading-edge and trailing-edge devices are deployed simultaneously, their effects on the lift coefficient are generally additive. The combination results in a higher overall lift coefficient and extends the range of operational angles of attack.

However, the interaction between the devices should be carefully considered, as improper placement or interaction can diminish the effectiveness of one or both. Ideally,

the deflections of both devices should complement each other to maximize aerodynamic performance [12].

High-lift devices are essential for enhancing an aircraft's aerodynamic performance, particularly during critical low-speed phases like takeoff and landing. Their influence on lift characteristics can significantly impact overall efficiency and operational capabilities. Several key aerodynamic benefits highlight the importance of high-lift system optimization:

- Increasing the lift coefficient ( $C_L$ ) by 0.10% at a fixed angle of attack reduces the required nose-up attitude during approach by approximately one degree. This can enhance handling characteristics and potentially allow for a more compact landing gear design.
- A 1.3% increase in maximum lift coefficient ( $C_{L,\max}$ ) corresponds to a 6,600 lb ( $\approx 3,000$  kg) increase in payload capacity while maintaining the same approach speed. This underscores how even small aerodynamic improvements can translate into significant operational benefits.
- A 1% increase in takeoff lift-to-drag ratio ( $L/D$ ) can extend the aircraft's range by approximately 150 nautical miles or allow for an additional 2,800 lb ( $\approx 1,270$  kg) of payload. This highlights the impact of efficient high-lift design on both fuel efficiency and payload capability.

These improvements emphasize the role of high-lift systems in maximizing aerodynamic efficiency. However, optimizing these devices requires balancing multiple design parameters to achieve higher lift without introducing excessive drag or undesirable flow characteristics [19].

The Fowler flap is designed to significantly improve the aerodynamic performance of an aircraft, particularly during takeoff and landing. It achieves this by moving rearward and then deflecting downward, creating a slot between the main wing and the flap, as shown in Figure 1.2. This allows the airflow to stay attached longer, which increases the lift generated by the wing. While the position and deflection of the flap are crucial, other aspects of its design, such as its shape and how it interacts with the main airfoil, are also important in determining its overall performance.

Several key parameters influence how well the Fowler flap works. For instance, the flap chord ratio ( $cf\_c$ ) determines the size of the flap relative to the wing, which affects how much lift can be generated. The conical curve extent ( $ce\_c$ ) controls the curvature along the flap's surface, influencing how smoothly the airflow transitions between the main wing and the flap. The shroud chord ratio ( $csr\_c$ ) helps to manage the airflow over the flap, while the shroud lip extent ( $clip\_ext$ ) impacts the flow's behavior near the wing's trailing edge. The flap leading-edge radius ( $r\_le\_flap$ ) plays a big role in how the air moves over the flap, affecting when and where the airflow will separate. Other factors like shroud tip thickness ( $tc\_shr\_tip$ ) and suction-side parameters ( $w\_conic$ ) help control the vortex

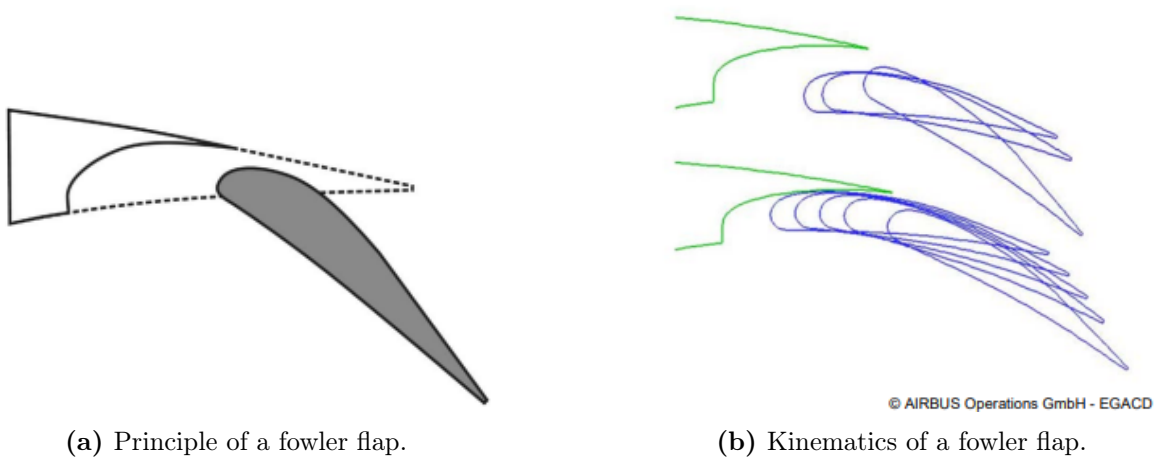


**Figure 1.2:** Mechanism of the fowler flap. Reproduced from [12], [18].

shedding and pressure distribution around the flap.

Another critical parameter is the flap deflection angle ( $\delta_f$ ), which as the name states, shows by how much the flap is deflected. For takeoff, this is set at 15 degrees, while for landing, it is increased to 30 degrees to provide the necessary lift for each phase of flight. The dimensions of the gap between the main wing and the flap, both in the x- and y-directions ( $x_{gap}$ ,  $y_{gap}$ ) (Figure 2.5), also play a role in the overall aerodynamic behavior, influencing flow attachment and separation.

Given the large number of parameters involved, designing the optimal Fowler flap requires a careful balancing act. Even small changes in any of these parameters can have a noticeable impact on the flap's performance. Therefore, understanding the influence of each parameter is essential to achieving the best aerodynamic results, particularly when considering the high-lift requirements for takeoff and landing.

### 1.3 Approach

This thesis investigates the aerodynamic performance of a Fowler flap for a Hybrid Laminar Flow Control (HLFC) airfoil using the PyAeroSweep tool-chain. The key components of this tool-chain include PyAeroSweep - a python-based computational fluid dynamics (CFD) tool, which leverages Fidelity Pointwise for meshing and SU2 for computational analysis of aerodynamic performance. By employing these tools, the system provides a robust framework to simulate and optimize high-lift configurations together with a drooped nose.

The primary aim is to conduct parametric studies on the Fowler flap design, with a specific focus on optimizing the aerodynamic flap design for deflection angles of - takeoff (15 degrees) and landing (30 degrees). The HLFC airfoil, developed through Dr.-Ing. Stanislav Karpuk's work at the SE<sup>2</sup>A (Sustainable and Energy-Efficient Aviation) cluster [20], serves as the basis for these simulations. The airfoil features a droop nose set at 15

degrees and is tested across various angles of attack to evaluate its aerodynamic behavior. Although the airfoil is designed for Hybrid Laminar Flow Control (HLFC), no active flow control (AFC) is employed during the simulations.

The tool-chain allows for the automatic setup of compressible steady Reynolds-Averaged Navier-Stokes (RANS) simulations with the  $k-\omega$  SST turbulence model in SU2, facilitating the analysis of lift and drag characteristics, as well as flow behavior, across different configurations. The workflow, implemented within the PyAeroSweep tool, automates mesh generation and computational fluid dynamic analysis, outputting results as .csv, .su2, and .vtu files. The aerodynamic metrics, such as  $C_L$  and  $C_D$ , are manually extracted from the .csv files and plotted, while flow visualization is performed using the .vtu files in Paraview.

This research aims to refine the flap's design configuration, enhancing its high-lift performance through an iterative approach of parameter variations and sensitivity analysis. The overall influence of these varied parameters on the aerodynamic performance is then discussed, with the presented results highlighting the achieved improvements in lift characteristics.

## 2 Methodology

### 2.1 PyAeroSweep

PyAeroSweep is a Python-based Computational Fluid Dynamics (CFD) analysis framework developed by Dr.-Ing. Stanislav Karpuk at the Institut für Flugzeugbau und Leichtbau (IFL). It integrates Fidelity Pointwise for automated meshing and SU2 to run CFD simulations. The framework currently supports steady-state Reynolds-Averaged Navier Stokes (RANS) simulations, utilizing either Sparat-Allmaras (SA) or the  $k-\omega$  Shear Stress Transport ( $k-\omega$  SST) model. The overall structure of PyAeroSweep is illustrated in Figure 2.1.

The PyAeroSweep framework provides multiple predefined test cases, as summarized in Table 2.1.

**Table 2.1:** Predefined test cases in PyAeroSweep.

Test Case	Description
Clean_airfoil_CST	Clean airfoil using CST parameterization
Clean_airfoil_Full	Full clean airfoil simulation
Flapped_airfoil_CST	Flapped airfoil using CST parameterization
Flapped_airfoil_PARSEC	Flapped airfoil using PARSEC parameterization
Full_3D_Wing	Full 3D wing aerodynamic analysis
LE_TE	Airfoil with leading-edge and trailing-edge devices
Mesh and Run	Automated meshing and simulation execution
Only RANS (solver)	SU2 simulation with steady RANS model only

The relevant modules and functionalities have been adapted to meet the specific simulation requirements of this thesis.

#### 2.1.1 Framework prerequisites

This framework relies on several prerequisites to function effectively.

- **Pointwise V18.6+:** A commercial software package used for generating high-quality computational meshes around complex geometries. PyAeroSweep utilizes Pointwise to create the discrete domain (meshes) necessary for running SU2 simulations.
- **SU2 v7.0+:** An open-source suite of computational analysis and design tool written in C++ and Python. PyAeroSweep leverages SU2 as its CFD solver to analyze the aerodynamic performance of the generated geometries.
- **preFoil:** Built upon pySpline, provides flexible handling of airfoil geometries, enabling tasks such as smooth interpolation, geometric modification, parameter computation, custom point distribution, and free form deformation (FFD) box generation for potential optimizations. As airfoil geometry manipulation is directly

relevant to this thesis, the baseline airfoil generated using this module is shown in Fig 2.2.

- **pyGeo:** a geometry manipulation package particularly suited for shape optimization, primarily employs a FFD approach to parametrize and deform geometries based on user-defined design variables, while also allowing imposing geometric constraints.
- **Open MPI:** Serves as the parallel computing framework, enabling PyAeroSweep to effectively run SU2 simulations across multiple processors, significantly reducing computational time for complex aerodynamic analysis.

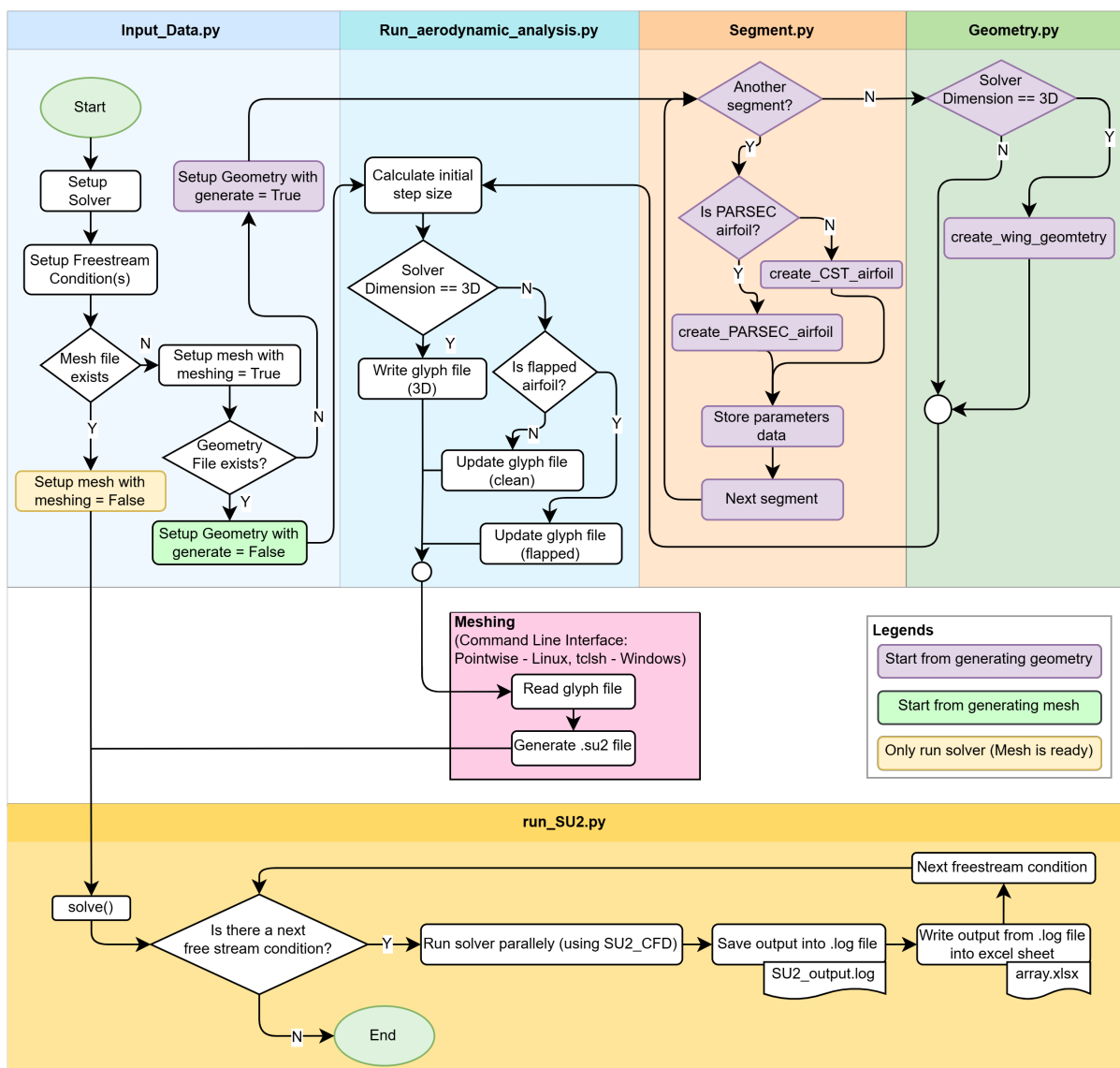
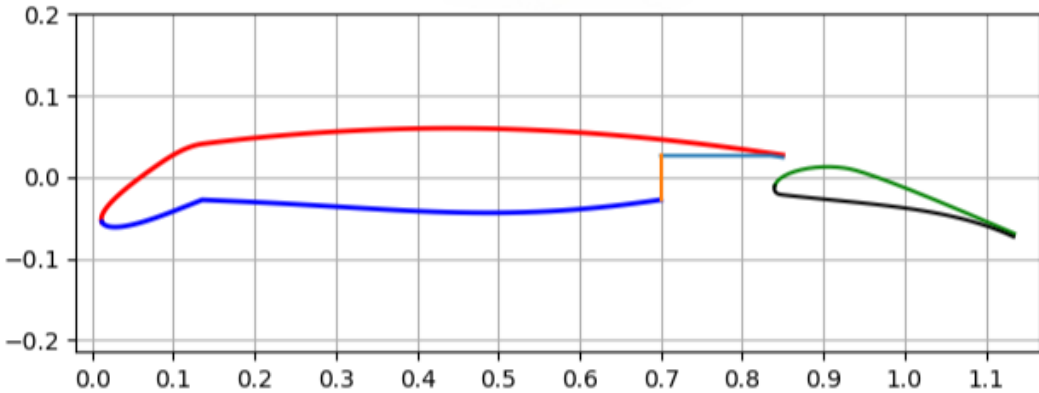


Figure 2.1: PyAeroSweep: Framework.



**Figure 2.2:** PARSEC Airfoil.

### 2.1.2 Workflow description

PyAeroSweep streamlines the aerodynamic analysis process by integrating geometry definition, mesh generation, flow solving, and post-processing. This section provides a general overview of its functionality, including specific details to show how it is used for the analysis of a flapped airfoil using PARSEC parameterization.

The complete input data script for this analysis, `Input_data_flapped_PARSEC.py`, is available in Appendix A. The general workflow of PyAeroSweep, as illustrated in Figure 2.1, is broken down into the following key stages:

1. **Initial setup and input data:** The process begins with the configuration of the aerodynamic solver and the specification of free stream conditions: Airspeed (in Mach), Altitude (in meters) and Angle of Attack (in degrees). For the flapped airfoil case, these parameters are defined in the `Input_data()` function. At this stage, PyAeroSweep checks for the existence of a pre-existing computed mesh file.
2. **Geometry definitions:**
  - **Mesh file does not exist:** PyAeroSweep proceeds to define the geometric model. It first checks if a geometry file exists. If not, the geometry file is generated based on user-defined parameters in `Geometry_data` within `Input_data()`. If a geometry file is present, it is loaded into the system. After the geometry is loaded, it moves on to mesh generation.
  - **Mesh file exists:** PyAeroSweep bypasses the geometry file generation steps and directly configures the meshing process using the existing file.
3. **Segment-based geometry preparation:** This stage focuses on defining the geometry of the airfoil, including the leading-edge droop nose and the trailing-edge flap, by processing each segment. PyAeroSweep determines the airfoil type (PARSEC or CST) for the main airfoil. For the flapped airfoil, both the main airfoil,

the leading-edge droop nose, and the trailing-edge flap are defined using PARSEC parameterization within the `Input_data()` function.

- The main airfoil geometry is created based on the PARSEC parameters specified in the `segment.Airfoil.PARSEC` dictionary.  
(Appendix B describes this dictionary, including CST.)
  - The leading-edge droop nose device, with its type set to 'Droop', is geometrically defined by the PARSEC parameters in `segment.LeadingEdgeDevice.PARSEC`.
  - The trailing-edge flap device, with its type set to 'Slotted', is geometrically defined by the PARSEC parameters in `segment.TrailingEdgeDevice.PARSEC`.
  - The geometric parameters for the airfoil, the droop nose, and the flap are stored.
  - An initial step size for the analysis is calculated.
  - A glyph file, which contains a script in Pointwise's native geometry definition language, is written to describe the PARSEC-defined main airfoil, the deflected droop nose, and the flapped configuration to Pointwise.
4. **Mesh generation for the flapped airfoil:** The glyph file describing the flapped airfoil geometry is used by Pointwise to generate a computational mesh. Pointwise is executed in batch mode, with the launch method differing by operating system (Linux: direct command-line execution of Glyph scripts; Windows: execution of Glyph scripts via `tclsh.exe`). The specific Glyph script for this flapped airfoil case is defined by `Mesh_data.glyph_file` in `Input_data()`. Pointwise processes the glyph file and the script to create the mesh around the geometry, and saves it as a '.su2' file.
  5. **Aerodynamic flow solving with SU2:** The generated '.su2' mesh file of the flapped airfoil serves as input for the SU2\_CFD solver, executed by the 'run\_SU2.py' script.
    - For each freestream condition defined in `Freestream` within `Input_data()` (including variations in Mach number, altitude, and angle of attack), the relevant parameters in the SU2 configuration file are modified.
    - For angle of attack (AoA) sweeps with a fixed flap deflection, the 'AoA' parameter is updated for each simulation, and the pre-generated mesh (`Mesh_data.filename`) is reused.
    - The solver is run, and for each condition, the results are written to a log file (`SU2_output.log`) within a case-specific folder as shown in Figure 2.3.  
(e.g., `Case_alt0.00_Mach0.21_AoA4.00`)
    - Importantly, SU2 also outputs solution files in the VTU format: `surface.vtu`, containing the computed flow field data on the airfoil surface, and `vol_solution.vtu`, containing the flow field data within the computational volume. These files are necessary for detailed flow visualization and analysis using post-processing software such as ParaView.

```

PyAeroSweep-main/
  Test_Cases/
    Flapped_airfoil_PARSEC/
      Geometry_files/
        flap_airfoil_lower.dat
        flap_airfoil_upper.dat
        main_airfoil_cut1.dat
        main_airfoil_cut2.dat
        main_airfoil_lower_1.dat
        main_airfoil_merged_31.dat
        main_airfoil_upper_1.dat
        parsec_airfoil.pdf
        parsec_airfoil.png
      Case_alt0.00_Mach0.00_AoA0.00/
        Case_alt0.00_Mach0.00_AoA0.00.cfg
        history.csv
        restart.dat
        su2meshEx.su2
        SU2_output.log
        surface.vtu
        vol_solution.vtu
      arrays.xlsx
      Input_data_flapped_PARSEC.py
      mesh_flapped_airfoil_SU2.glf
      Run_airfoil_template.cfg

```

**Figure 2.3:** PyAeroSweep - Flapped airfoil PARSEC folder.

6. **Iterative analysis for multiple freestream conditions:** PyAeroSweep systematically iterates through all the defined freestream conditions in **Freestream**.
  - For each condition, the flow solver (SU2) is executed using the appropriate configuration settings (e.g., updated ‘AoA’).
  - The solver operates on the computed mesh, and the output (log files and VTU files) is saved in a separate case folder corresponding to that specific freestream condition.
  - This ensures that the aerodynamic performance is evaluated across the entire range of pre-specified analysis conditions.
7. **Post-processing of results:** After the flow solver completes the analysis for all specified freestream conditions, the output log files from each case folder are processed.
  - Relevant aerodynamic data, such as lift, drag, and momentum coefficients, are extracted and organized into a structured format, in an Excel spreadsheet (array.xlsx).
  - Additionally, each case-specific folder has an Excel spreadsheet (history.csv) with detailed information on relevant aerodynamic data for the entirety of the simulation iterations.
  - This facilitates quantitative analysis, visualization of integrated quantities, and comparison of the flapped airfoil’s performance across the simulated conditions.

- The detailed flow field data contained in the VTU files (generated by SU2 for each condition) is then further analyzed and visualized using dedicated post-processing software like ParaView to gain deeper insights into the flow physics and to generate visual representations of the aerodynamic phenomena.

### 2.1.3 Geometry definition

The effective design of a high-lift system depends on how accurate and effective the complex flap geometries are parametrized. This requires balancing several factors: the flexibility to represent various shapes, precise control over important geometric features, and reducing the number of design variables. These challenges have been addressed by developing a flap parametrization method [21], that combines circular arcs (green) (as illustrated in Figure 2.4b), conical curves (blue), and spline curves (red), as represented in Figure 2.4a. This approach allows for the creation of realistic flap shapes with a relatively small set of parameters.

In this method, the flap profile is constructed in a series of steps. A circular arc is employed at the flap's leading edge to control the initial curvature, which directly influences the leading edge flow separation. A conical curve segment is then used to smoothly connect this arc to the main portion of the flap, providing control over thickness distribution, as illustrated in Figure 2.4b. Finally, a spline curve, which is constructed using Bezier segments, is used to blend the conical curve into the flap's upper surface, which ensures smooth transition and avoids discontinuities. The parameters governing these curves such as conical curve parameter `w_conic` and extent `ce_c`, and the shroud lip extent `clip_ext`, represented in Table 2.2, directly influence the flap's overall shape and also its aerodynamic performance.

Although the underlying principles of the flap shape parametrization are derived from [21], a key enhancement has been made to provide more control over the flap setting. PyAeroSweep explicitly incorporates the parameters: (a) the horizontal `x_gap` and (b) the vertical `y_gap` distances between the shroud and the flap, as illustrated in Figure 2.5. These parameters offer a straightforward way to control the slot geometry, which influences the channel flow, which is crucial for optimizing the flow through the gap and for maximizing the effectiveness of the flap system. Additionally, the flap deflection, another essential setting parameter, is defined geometrically by the angle formed between the chord line of the main airfoil and the chord line of the flap. Table 2.2 showcases the parameters of the Fowler flap with the baseline values.

### 2.1.4 Mesh generation

The computational mesh for the flapped airfoil is generated using Pointwise, a commercial meshing software. Considering the geometric complexity introduced by the flap and the requirement for accurate resolution of viscous effects near the flap surface, an unstructured hybrid meshing strategy is employed.

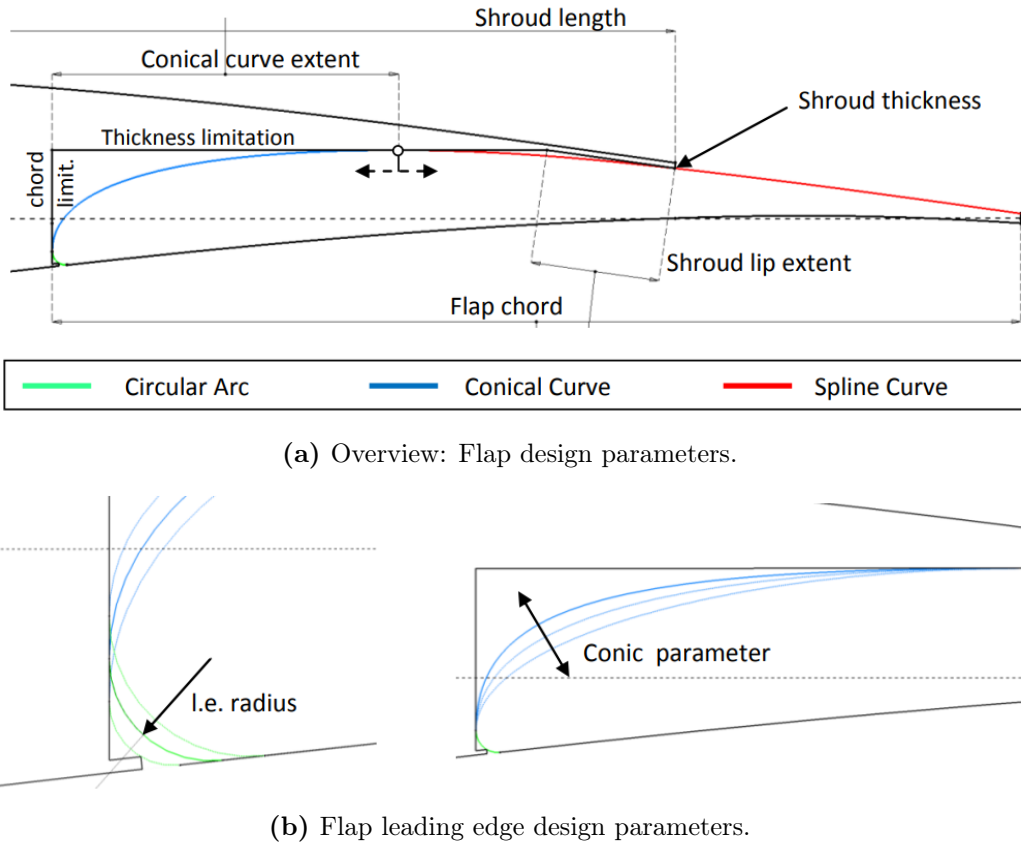


**Figure 2.4:** Key flap geometry definitions. Reproduced from [21].

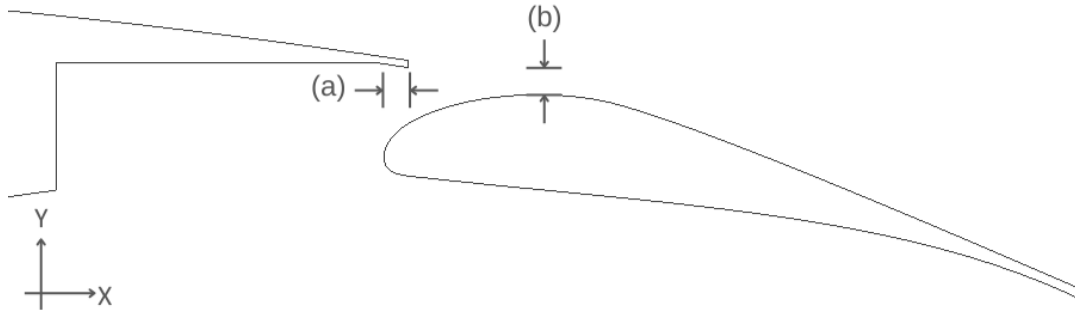


**Figure 2.5:** (a) Horizontal overlap  $x\_gap$  and (b) Vertical gap  $y\_gap$  definitions.

This hybrid approach utilizes an unstructured mesh as the foundation for discretizing the computational domain. Unstructured meshes, composed primarily of triangles in 2D (as seen in Figure 2.6 and the detailed view around the flap in Figure 2.7), offer the flexibility necessary to capture the complex geometric features of the airfoil, including the flap, shroud, and other geometric discontinuities present at their points of interaction. The distribution and clustering of points on the mesh edges are controlled via a Pointwise Glyph script (.glf), enabling automated refinement within PyAeroSweep. Parameters such as the desired  $Y+$  value, far-field dimensions, and airfoil mesh parameters such as T-Rex

(Turbulence-Resolving Extruder) layers can be changed within `Input_data()` allowing for ease of meshing. (refer to Appendix A: MESH SETTINGS)

**Table 2.2:** Geometric parameters for the baseline flap design.

(a) Parameters defined with respect to the airfoil chord.

Parameter	Notation	Baseline (ratios)
Flap chord ratio	cf_c	0.3
Shroud chord ratio	csr_c	0.85
Shroud tip thickness	tc_shr_tip	0.003
X-Gap	x_gap	0.01
Y-Gap	y_gap	0.005

(b) Parameters defined with respect to the flap chord.

Parameter	Notation	Baseline (ratios)
Shroud lip extent ratio	clip_ext	0.05
Conical curve extent ratio	ce_c	0.3
Flap leading edge radius	r_le_flap	0.01
Conical parameter	w_conic	0.5
Flap deflection	delta_f	15°/30°

While unstructured meshes are preferred for representing complex shapes, accurately resolving the boundary layer requires specific treatment of the near wall region. To achieve this within the unstructured framework, Pointwise's T-Rex (Turbulence-Resolving Extruder) technique is employed. T-Rex generates layers of cells adjacent to the airfoil and flap surfaces that exhibit a controlled gradient of anisotropy. In the present mesh, immediately next to the surface, the prism cells are extremely stretched along the surface and highly compressed in the direction normal to it (as illustrated in Figure 2.6 and Figure 2.7). This high aspect ratio is crucial for effectively capturing the large gradients in flow variables such as velocity, pressure and temperature within the very thin viscous sub-layer. As these extruded layers progress away from the surface, the cells gradually become less stretched and more equiangular, eventually transitioning smoothly to predominantly triangular cells of the outer unstructured domain. This approach enables the benefit of an unstructured mesh's flexibility for complex geometry while incorporating highly anisotropic cells near the walls for accurate viscous flow resolution, as facilitated by Pointwise's T-Rex algorithm.

Pointwise's computational mesh generation for this viscous sub-layer using the T-Rex feature required three key parameters: the Number of Layers, Growth Rate and the Initial Step Size. The Number of Layers and Growth Rate are user-defined options specified within the MESH SETTING section of the code (refer to Appendix A: MESH SETTINGS). The Initial Step Size  $\Delta_s$ , representing the height of the first cell adjacent to the wall is calculated internally in the PyAeroSweep framework through a specific Python module.

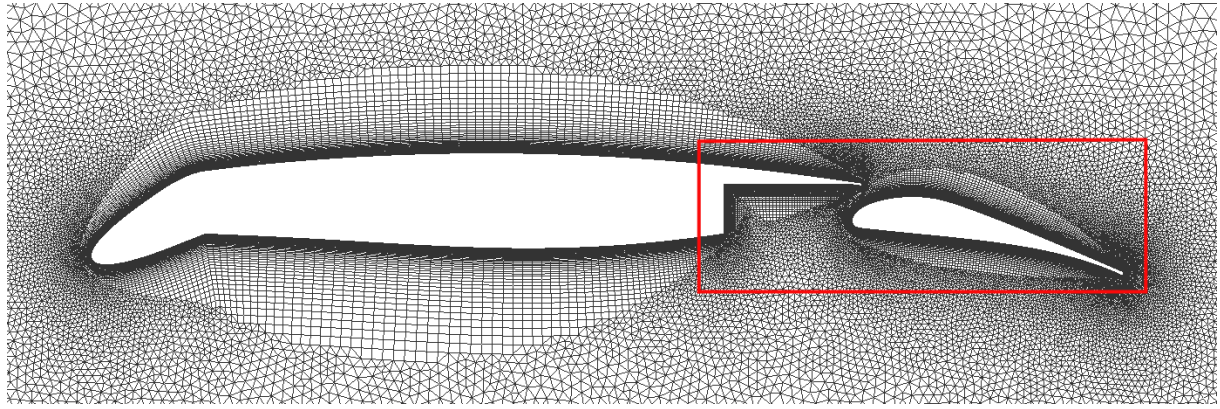


**Figure 2.6:** Computational mesh around the HLFC airfoil.

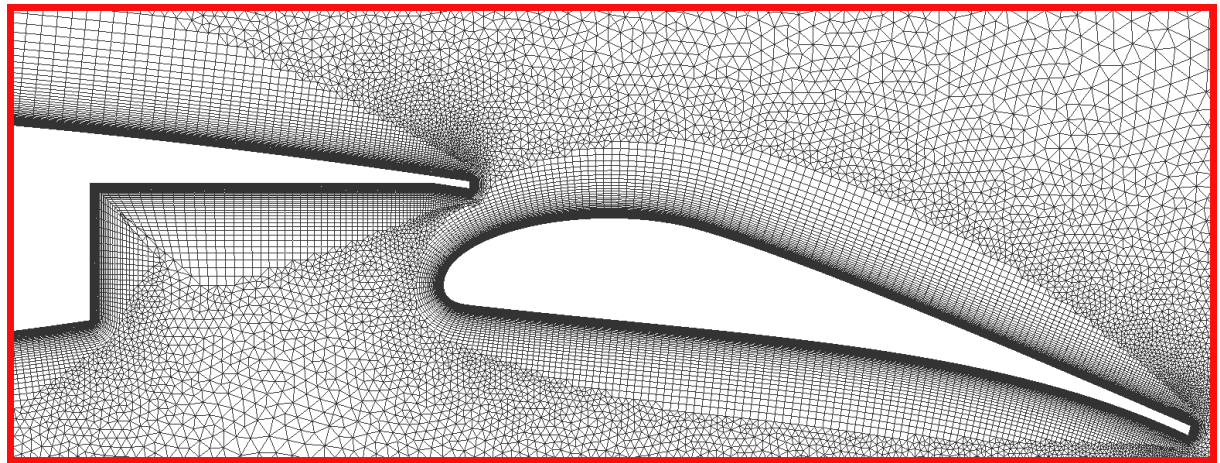


**Figure 2.7:** Detailed view of the computational mesh around the Fowler flap.

This module also uses the desired dimensionless wall distance  $Y^+$  which is also provided as a user input in the MESH SETTING section. To calculate the  $\Delta_s$ , the module first accounts for the atmospheric conditions based on the International Standard Atmosphere (ISA). This also involves calculating the local pressure  $P$ , temperature  $T$ , and density  $\rho$  as a function of altitude.

Additionally, the free stream velocity ( $U_\infty$ ) is determined from the given free stream Mach Number ( $Ma$ ) and the dynamic viscosity ( $\mu$ ) of the air is computed based on the ISA temperature. The Reynolds number ( $Re_x$ ) is calculated using the free stream conditions and a characteristic length (airfoil chord).[22]

The code further estimates the friction coefficient ( $C_f$ ) using Equation (2.1) based on the Reynolds number ( $Re_x$ ) assuming a flat plate.

$$C_f = \frac{0.026}{Re_x^{1/7}} \quad (2.1)$$

The wall shear stress ( $\tau_{wall}$ ), representing the frictional force per unit area at the wall, is calculated using Equation (2.2), incorporating the skin friction coefficient ( $C_f$ ), fluid density ( $\rho$ ), and freestream velocity ( $U_\infty$ ).

$$\tau_{wall} = \frac{C_f \rho U_\infty^2}{2} \quad (2.2)$$

Equation (2.3) defines the friction velocity ( $U_{fric}$ ), a characteristic velocity scale in the turbulent near-wall region, derived from the wall shear stress ( $\tau_{wall}$ ) and fluid density ( $\rho$ )

$$U_{fric} = \sqrt{\frac{\tau_{wall}}{\rho}} \quad (2.3)$$

The Initial Step Size ( $\Delta_s$ ), the height of the first computational cell adjacent to the wall is calculated using the equation (2.4). This equation directly utilizes the dimensionless wall distance ( $Y^+$ ), along with the dynamic viscosity ( $\mu$ ), friction velocity ( $U_{fric}$ ), and fluid density ( $\rho$ ), to determine the appropriate resolution near-wall grid.

$$\Delta_s = \frac{Y^+ \mu}{U_{fric} \rho} \quad (2.4)$$

The generation of this carefully constructed hybrid mesh, with its tailored resolution around the flapped airfoil, provides the necessary foundation for subsequent CFD simulations. This detailed meshing strategy ensures that the complex flow features, particularly around the flap, can be resolved to the best of the solver's abilities.

### 2.1.5 Numerical solver and simulation setup

The aerodynamic analysis of Fowler flap configurations relies on numerical simulation performed with the SU2 CFD suite, integrated within PyAeroSweep framework. This framework automates the process of generating SU2 configuration files (Figure 2.3 - `Run_airfoil_tempelate.cfg`) executing the solver for various freestream conditions and extracting the resulting aerodynamic coefficients.

It is important to note that the current setup inside PyAeroSweep utilizes and is limited to steady-state Reynolds-Averaged Navier-Stokes (RANS) simulations.

The steady RANS equations were solved to model the mean flow field around the airfoil and flap. Turbulence closure was achieved using the  $k - \omega$  SST (Shear Stress Transport) model, as defined in the configuration file (refer to Appendix C). The working fluid was treated as standard air with temperature-dependent viscosity and constant Prandtl numbers for laminar and turbulent flows.

The  $k - \omega$  SST model is a two-equation model that combines the advantages of the  $k - \omega$  model in the near-wall region with the  $k - \epsilon$  model in the freestream. The model solves the transport equations for the turbulent kinetic energy  $k$  and specific dissipation rate  $\omega$  [23][24]. This hybrid approach makes it particularly well suited for aerodynamic flows involving adverse pressure gradients and separations, which are prevalent around

deployed high-lift devices such as Fowler flaps.

SU2 offers the Spalart-Allmaras (SA) model as another option for turbulence modeling of aerodynamic flows. The SA model is a one-equation model known for its computational efficiency. However, the two-equation  $k - \omega$  SST model was selected due to its better capabilities in predicting complex flow features in and around the Fowler flap. Some of the important considerations and differentiating points in making this decision were:

- **Handling of adverse pressure gradients and flow separation:** The SST model provides a more accurate prediction of flow separation and effects of adverse pressure gradients on the upper surface of the airfoil and flap, and in the gap region, whereas SA lags in performance and accuracy in such scenarios.
- **Near-wall resolution:** The  $k - \omega$  formulation allows for the direct integration to the wall with a sufficiently fine mesh, which offers a more accurate representation of the boundary layer development, near-wall viscous layer, and its influence on flow separation compared to the wall function approach of the SA model.

The spatial discretizations of the governing equations are performed using the Finite Volume Method (FVM), a numerical technique that divides the domain into a finite number of control volumes and solves the integral form of the conservation equations over each volume. This ensures that the fundamental laws (such as conservation of mass and momentum) are satisfied within each cell. To achieve a balance between accuracy and stability, specific numerical schemes were used to calculate the flow properties at the boundaries between the cells. These schemes were designed to minimize errors and prevent unrealistic oscillations in the solution.

The computational domain was bounded by specific conditions to simulate the interaction of the airflow with the physical geometry, and the far-field environment. On the surface of the airfoil and the flap, a "no slip wall" condition was applied. This means that the layer of air directly in contact with the surface has zero velocity relative to the surface validating the aerodynamic principle assumptions of viscous effects. Additionally, an "adiabatic wall" condition was used, meaning no heat transfer between the airflow and surfaces of the airfoil and flap. Far away from these components, a "far-field" condition was used to represent the undisturbed freestream airflow.

Since the focus was on the steady solution, i.e. the final state of the airflow, a numerical technique was used to advance the solution through a series of "pseudo-time" steps until it no longer showed variations. Advanced mathematical methods were used to speed up this process in order to reach the final solution efficiently through the parameters defined in the configuration file (refer to Appendix C).

To determine the stage in which the simulation has reached a stable and reliable solution, convergence criteria were used, which included monitoring the residuals of the flow equations. Additionally, a Cauchy convergence criterion was used, specifically on the lift coefficient. This criterion assesses the relative change in the lift coefficients between

successive iterations. In the case of the present study, SU2 monitored the lift coefficient over the last `CONV_CAUCHY_ELEMS= 500` elements. Convergence was achieved for this criterion when the average relative change in the lift coefficient over these 500 elements fell below a user-defined tolerance `CONV_CAUCHY_EPS= 5e-07`, and this monitoring is started after the initial `CONV_STARTITER= 10` iterations. This approach helps to ensure that the lift force has stabilized and is no longer significantly fluctuating, indicating a converged aerodynamic solution. Additional stopping conditions such as the minimal residual target `CONV_RESIDUAL_MINVAL` and a maximum iteration limit `ITER= 25000` were also used.

### 2.2 Concluding remarks

The described methodology ensures a structured and reliable aerodynamic evaluation of the Fowler flap configuration. The combination of automated geometry generation, meshing and CFD simulation within PyAeroSweep streamlines the analysis, while the  $k - \omega$  SST turbulence model allows for accurate prediction of flow behaviors, including adverse pressure gradients and separation characteristics. Furthermore, the implemented convergence criteria ensure numerical stability, minimizing fluctuations and uncertainties in the obtained results.

Building on this foundation, the following section presents the trade studies conducted to systematically refine the flap design, starting from the baseline configuration.

## 3 Trade Studies

### 3.1 Fowler flap design optimization strategy

The optimization of the Fowler flap design was conducted through a systematic trade study approach, the workflow of which is illustrated in Figure 3.1. The analysis began with predefined HLFC airfoil parameters, which remained constant throughout the study. The core of the optimization involved iteratively adjusting and evaluating various flap parameters to maximize the lift coefficient ( $C_{L_{max}}$ ).

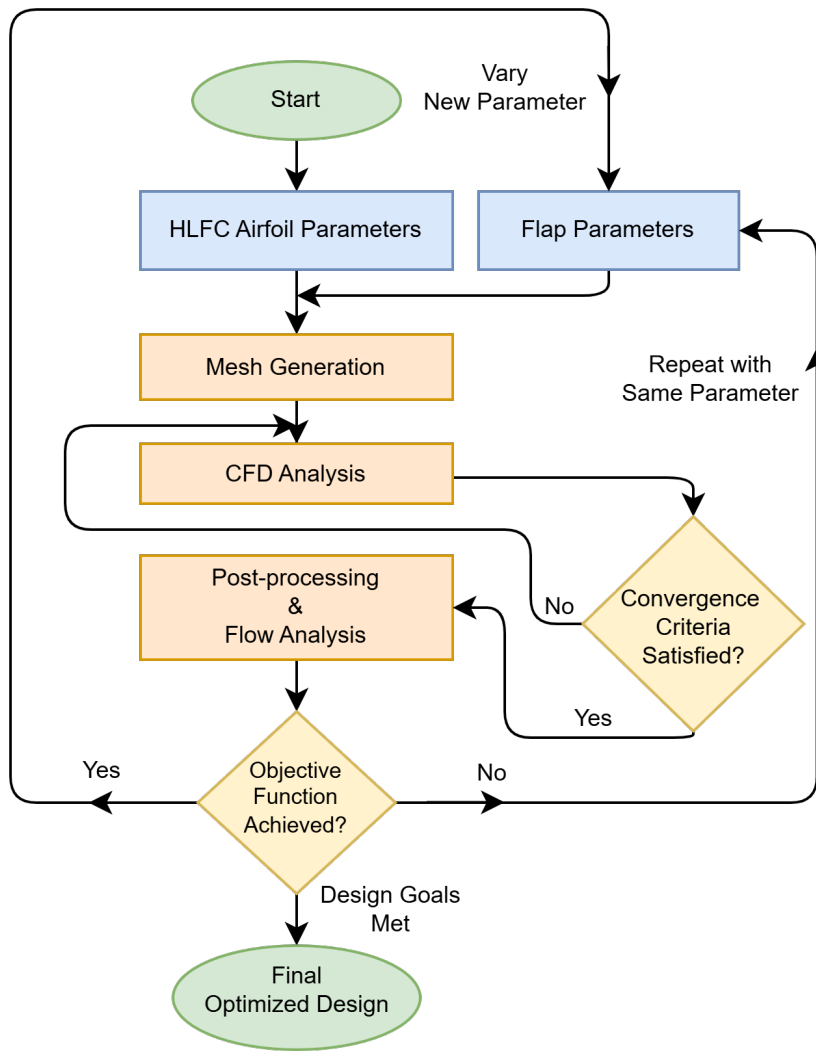


**Figure 3.1:** Fowler flap design optimization strategy.

A mesh sensitivity study was performed to establish the best mesh for accurate evaluation of aerodynamic characteristics throughout the optimization process, before the parameter sensitivity study. The parameter sensitivity study employed a One-At-A-Time (OAT) optimization strategy, where individual flap parameters were varied across defined ranges while other parameters were held constant, isolating this parameter to assess their

impact on the aerodynamic performance.

For each set of flap parameters, a computational mesh compatible with SU2 (.su2) was generated using the previously explained PyAeroSweep routine through Pointwise. This mesh served as the foundation for the following CFD analysis using the SU2 solver. The simulations were run until predefined convergence criteria were met.

Following convergence, the aerodynamic performance, specifically the lift coefficient was evaluated. The process then determined if the objective had been achieved within the explored range of each of the parameters. The "Vary New Parameter" block in the flowchart represents the selection of the next flap parameter upon achieving the objective. If the optimal lift was not found within the current range of values or if further improvement seemed possible, the analysis would move onto a new routine, focusing on adjusting the same parameter with a refined range of values using the "Repeat with Same Parameter" block. Once this was achieved, the OAT cycle would move on to the next parameter and its range of values. This iterative loop was continued until a satisfactory level of lift maximization was achieved.

### 3.1.1 Mesh sensitivity study

A mesh sensitivity study was conducted prior to the parameter sensitivity study to determine the optimal mesh refinement required to balance accuracy and computational cost during the simulation. This was performed by analyzing the influence of the mesh refinement on the maximum lift coefficient ( $C_{L_{\max}}$ ) using three levels of mesh density : Coarse, baseline, and fine. The choice of these mesh types was aimed at evaluating the impact of cell count on the accuracy of the aerodynamic simulation prediction.

The results of the mesh sensitivity study, presented in Table 3.1, indicate that a refinement of the mesh from coarse to baseline results in a 0.71% increase in  $C_{L_{\max}}$ , making it a significant improvement. However, further refinement from baseline to fine only improves  $C_{L_{\max}}$  by 0.27% despite a 23% increase in the number of cells and a 30% increase in the connector dimensions. This trend of diminishing improvement suggests that further refinement provides limited aerodynamic accuracy but comes at a substantial increase in computational effort.

**Table 3.1:** Results of the mesh sensitivity study.

Mesh Type	Cell Count	Connector Scaling	$C_{L_{\max}}$
Fine	138,244	+30%	2.956
Baseline	111,992	Baseline	2.948
Coarse	84,225	-30%	2.927

Figure 3.2 illustrates the variation of  $C_{L_{\max}}$  with the number of mesh cells (divided by 1000) for each mesh type, with the y-axis representing the corresponding values of  $C_{L_{\max}}$ . As expected, the curve demonstrates that  $C_{L_{\max}}$  increases with mesh refinement. However,

the gradient of increment decreases beyond the baseline mesh, emphasizing diminishing returns on further refinement.

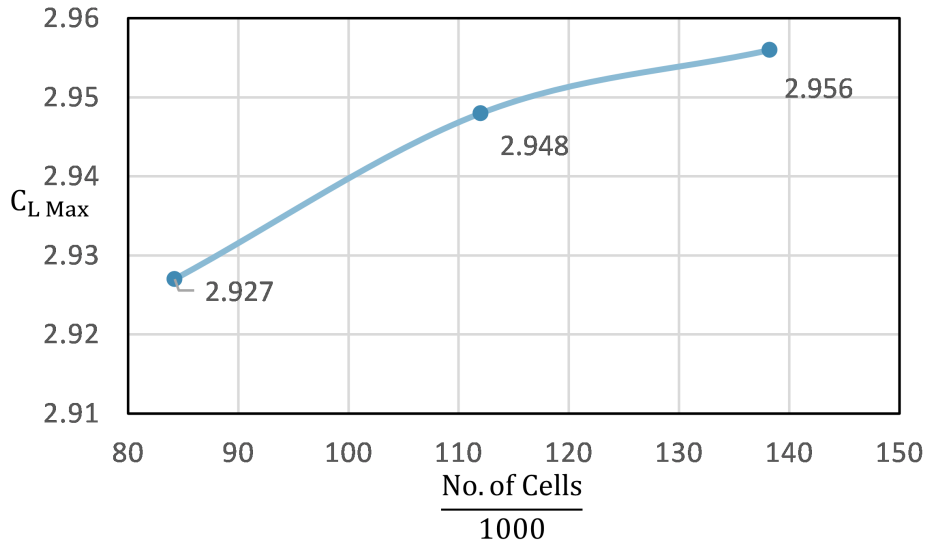


**Figure 3.2:** Impact of mesh refinement on maximum lift coefficient ( $C_{L_{\max}}$ ).

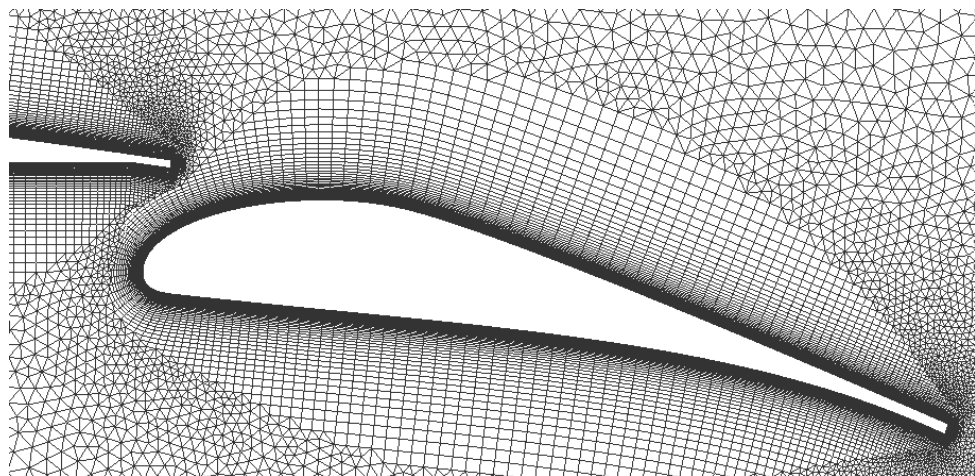
While the coarse mesh under-predicts the  $C_{L_{\max}}$  by 0.71%, the finer mesh showcases an improvement of only 0.27% compared to the baseline mesh, despite its increases computational burden. This indicates that the baseline mesh is already capable of capturing the essential aerodynamic characteristics for the purpose of this study.

Figure 3.3 illustrates the qualitative refinement process by showing the transition from coarse to the fine mesh topology.

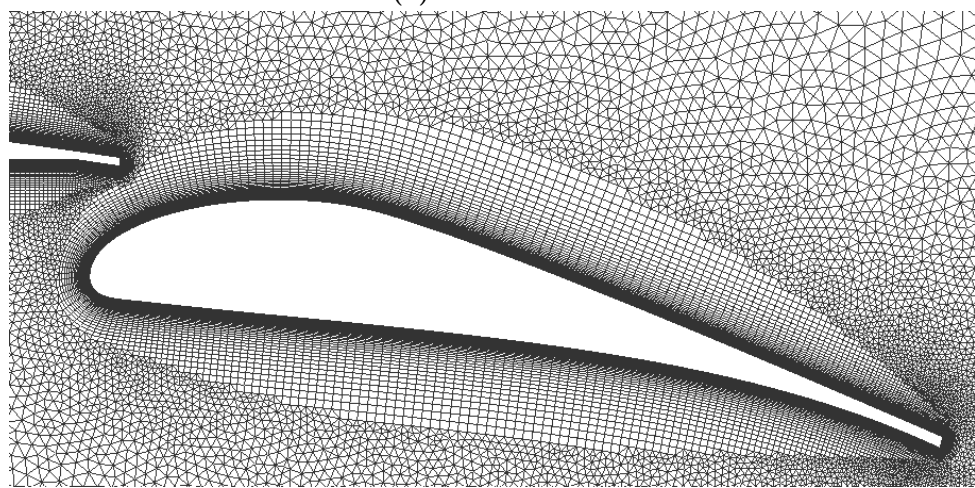
Given the need to perform extensive parameter sweeps as part of the optimization study, along with the computational limitation of the available hardware, the baseline mesh was chosen as the most practical option. It offers an optimal trade-off between accuracy and computational efficiency.

It is also important to note that these simulations were performed using steady-state Reynolds-Averaged Navier-Stokes (RANS) approach with  $k - \omega$  SST (Shear Stress Transport) model. The SST model is known for its improved performance in capturing adverse pressure gradients and flow separations. However, being a steady formulation, it lacks the ability to resolve unsteady flow phenomena such as vortex shedding and dynamic stall.

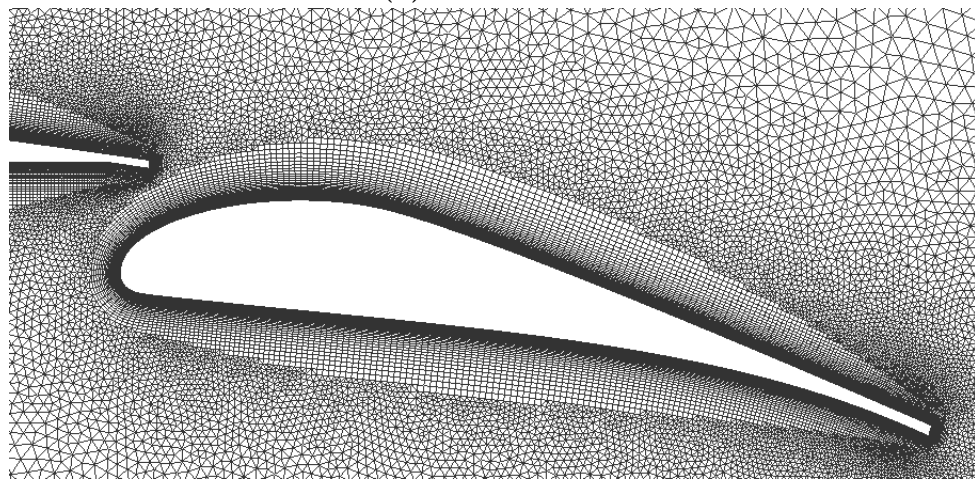
Therefore, while further mesh refinement could marginally improve accuracy, its benefits are limited within the context of steady RANS simulations, and the baseline mesh remains the most practical and robust choice for the present study.



(a) Coarse mesh.



(b) Baseline mesh.



(c) Fine mesh.

**Figure 3.3:** Effect of mesh refinement on grid resolution.

### 3.1.2 Parameter sensitivity study

To determine the optimal flap configuration for maximizing the lifting characteristic during takeoff and landing, a parameter sensitivity study was conducted using One-At-A-Time (OAT) optimization method. High-lift devices such as the Fowler flap are crucial for generating increased lift at reduced speeds associated with these flight phases. Therefore, the flap parameters were evaluated for two distinct flap deflection angles: 30 degrees, representative of the landing configuration, and 15 degrees, typical for takeoff [25] with the given freestream conditions as illustrated in Table 3.2.

The OAT process involved systematically varying each parameter individually while keeping other flap parameters fixed at the baseline or the current best-known values, separately for each flap deflection angle. The aerodynamic analysis was performed across a sweep of the angle of attacks: 4, 6, 8, 10, 11, 12, 13, 14, and 15 degrees. The larger initial gap between the lower angles of attack (4 to 10 degrees) was sufficient for capturing the general trends at lower lift coefficients. However, as higher angles of attack are approached (10 to 15 degrees), where the flow behavior becomes more critical for maximum lift and stall characteristics, the angle of attack step size was reduced to 1 degree to capture these with greater precision. In particular, the subtle changes in the contour of the lift coefficient  $C_L$  curves, as seen in Figure 3.4 (around  $\alpha = 10^\circ$ ), indicate that even small variations in the step size lead to a noticeable change in the contour.

**Table 3.2:** Simulation freestream conditions and reference length (airfoil chord).

Parameter	Value	Units
Mach Number ( $Ma$ )	0.21	-
Altitude	0	meters (Sea Level)
Angle of Attack ( $\alpha$ )	4, 6, 8, 10, 11, 12, 13, 14, 15	degrees
Reference Length ( $C$ ) (Airfoil Chord)	3.28	meters

The OAT process proceeded as follows for each deflection angle:

- An initial set of baseline values for flap parameters was provided, yielding baseline aerodynamic characteristics.
- One flap parameter was selected for variation.
- This selected parameter was varied across a predefined range of values, while all other flap parameters remained constant, throughout the angle of attack sweep.
- For each value of the varied parameter and each angle of attack, a complete simulation was performed and the aerodynamic coefficients were evaluated.
- The value of the varied parameter that yielded better lift characteristics across the angle of sweep within the tested range was identified as the, locally "optimal" value for that parameter.

- The baseline of this parameter was then updated to this locally optimal value.
- This process was repeated by selecting the next flap parameter and varying it across its range, keeping all other parameters fixed throughout the angle of attack sweep.
- This cycle of varying one parameter at a time was continued for all the defined flap parameters across their respective range and throughout the angle of attack sweeps.

A visual overview of this process is illustrated in the flowchart in Figure 3.1 and Table 3.3 represents the list of parameters for the baseline configuration with the baseline values for each parameter. Initial investigation revealed a greater sensitivity of the lift coefficient to flap parameter variations at 30-degree flap deflection compared to 15 degrees. Consequently, the focus was shifted towards the 30-degree flap deflection. Notably, the horizontal overlap (**x\_gap**) and vertical gap (**y\_gap**) showed greater sensitivity to the changes in the lift coefficient ( $C_L$ ) compared to other parameters.

The range for the geometric parameters explored in this study, as summarized in Table 3.3, were determined based on a combination of prior research and geometric feasibility. The baseline configuration utilized a **x\_gap** of 3.0% and a **y\_gap** of 1.5% of the airfoil chord. Subsequently **x\_gap** was systematically varied from 0.3% to 4.3% of the airfoil chord. This specific range was selected based on prior experimental evidence demonstrating that an **x\_gap** of 4.3% optimizes lift generation when the flap is deflected to 30 degrees for a slotted flap [26]. While the current study is focused on the aerodynamic design optimization of a Fowler flap, this prior research provides a valuable starting point. Similarly, the **y\_gap** was varied from 2.3% to 10% of the airfoil chord with the lower limit of 2.3% also determined by previous research indicating its favorable effect on lift characteristics [26].

The Flap chord ratio **cf\_c** range of 0.2 to 0.3 based on typical values for effective high-lift flaps [27], and the flap deflection range of 15° to 30° was selected to replicate the relevant takeoff and landing conditions [28]. For the remaining geometric parameters - Conical curve extent ratio (**ce\_c**), Flap leading edge radius (**r\_le\_flap**), Conical Parameter (**ce\_c**) and Shroud lip extent ratio (**clip\_text**) normalized with respect to the flap chord (Table 3.3b), and Shroud chord ratio (**csr\_c**) and Shroud tip thickness (**tc\_shr\_tip**) are normalized with respect to the airfoil chord (Table 3.3a), whose range of values were established through visual assessment to ensure practicality, allowing for an in-depth exploration of their impact on aerodynamic performance.

To isolate the individual effects of the **x\_gap**, and the **y\_gap**, a two-step approach was employed. The influence of the **x\_gap** was assessed while keeping the **y\_gap** constant at 4% of the airfoil chord. Subsequently, the **y\_gap** was varied while keeping the **x\_gap** constant at 4.3% of the airfoil chord. This systematic analysis facilitated in determining the individual contribution of each parameter to overall aerodynamic behavior, as represented in the aerodynamic coefficient graphs in Figure 3.4 and Figure 3.5. The following analysis will examine these coefficients and correlate them with the flow visualization data shown

**Table 3.3:** Range of geometric parameters for the to-be optimized flap design.

(a) Parameters defined with respect to the airfoil chord.

Parameter	Notation	Baseline	Range (ratios)
Flap chord ratio	cf_c	0.3	0.2, 0.25, 0.3
Shroud tip thickness	tc_shr_tip	0.003	0.003, 0.005, 0.007
Shroud chord ratio	csr_c	0.85	0.8, 0.85, 0.9
X-Gap	x_gap	0.01	0.0075, 0.0108, 0.0141
Y-Gap	y_gap	0.005	0.0131, 0.0164, 0.0197

(b) Parameters defined with respect to the flap chord.

Parameter	Notation	Baseline	Range (ratios)
Shroud lip extent ratio	clip_ext	0.05	0.0, 0.025, 0.05
Conical curve extent ratio	ce_c	0.3	0.2, 0.3, 0.35
Flap leading edge radius	r_le_flap	0.01	0.01, 0.0135, 0.017
Conical parameter	w_conic	0.5	0.5, 0.75, 1.0
Flap deflection	delta_f	15°/30°	15°, 30°

in Figure 3.6 and Figure 3.7 to provide a comprehensive understanding of how these parameters affect the flow physics and high-lift performance.

- **Effect of variation of  $y\_gap$  on  $C_D$  and  $C_L$  varied across  $\alpha$ :**

Figure 3.4 shows the impact of varying  $x\_gap$  while maintaining a fixed  $y\_gap$  of 4.0%. As seen in Figure 3.4a, the 2.3%  $x\_gap$  configuration (green line) stands out by achieving the highest maximum lift coefficient ( $C_{L_{max}}$ ). This suggests a potential for enhancing the aerodynamic performance. Figure 3.4b reveals a slight increase in drag associated with the 2.3%  $x\_gap$ , particularly at higher angles.

Examining the flow visualization at a low AoA of 4 degrees, Figure 3.6b shows that the 2.3%  $x\_gap$  configuration exhibits a less disturbed flow over the flap compared to the baseline in Figure 3.6a, which displays a more developed eddy viscosity at the flap's leading edge. This shows that while the 2.3%  $x\_gap$  might not provide the highest lift at very low AoA, it has a more favorable flow structure for lift development as the angle of attack increases.

- **Effect of variation of  $x\_gap$  on  $C_D$  and  $C_L$  varied across  $\alpha$ :**

Figure 3.5 explores the influence of variation of  $y\_gap$  with a fixed  $x\_gap$  of 4.3%. The lift coefficient plot in Figure 3.5a indicates that the 6%  $y\_gap$  configuration (green line) yields favorable lift coefficients throughout the angle of attack range, with a distinct advantage at higher angles. Furthermore, the lift versus drag coefficient plot in Figure 3.5c showcases a performance trend for the 6%  $y\_gap$  that closely resembles the baseline with a notable improvement in the lift-to-drag ratio becoming apparent at higher lift coefficients. This advantage becomes more appar-

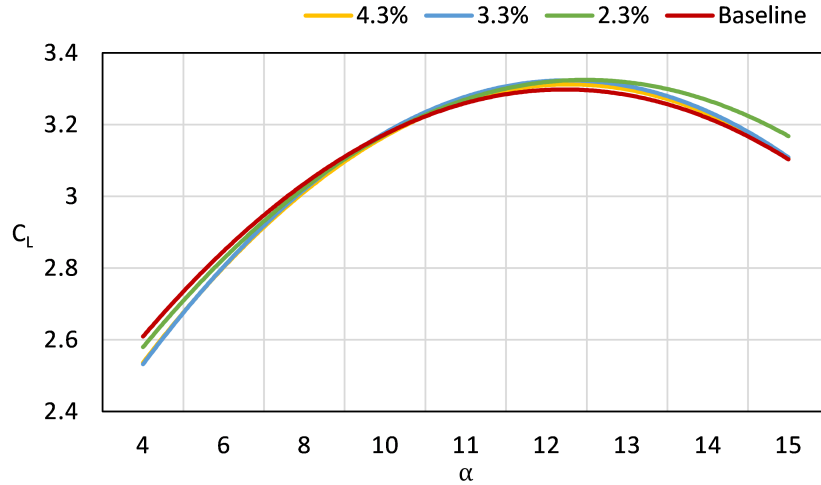
ent at higher angles of attack. The corresponding drag characteristics are illustrated in Figure 3.5b.

Flow visualization at a lower AoA of 4 degrees as represented in Figure 3.6c shows that the 6% *y\_gap* promotes a smooth flow over the flap with reduced eddy viscosity. This favorable flow behavior is also evident at a higher AoA of 13 degrees in Figure 3.7c where the 6% *y\_gap* exhibits a less extensive region of high eddy viscosity compared to the baseline in Figure 3.7a. This suggests that increasing the *y\_gap* to 6% helps maintain a more attached flow and delays separation, contributing to sustained lift performance.

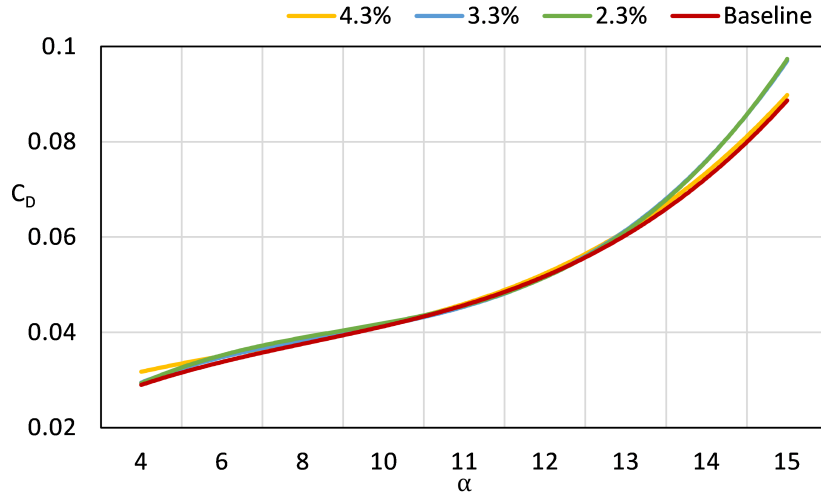
Considering the observation from both the aerodynamic coefficients and the flow visualizations, the combination of 2.3% *x\_gap* and 6% *y\_gap* appears to offer a favorable balance. The 2.3% *x\_gap* excels in maximizing  $C_{L_{max}}$  and provides good lift-to-drag characteristics, while the 6% *y\_gap* showcases improved flow characteristics, particularly reduced eddy viscosity, at both low and high AoA, potentially enhancing lift generation and delaying separation. There, this combination utilizes the strengths of each parameter setting to achieve enhanced high-lift performance in the required flight envelopes.

### 3 Trade Studies

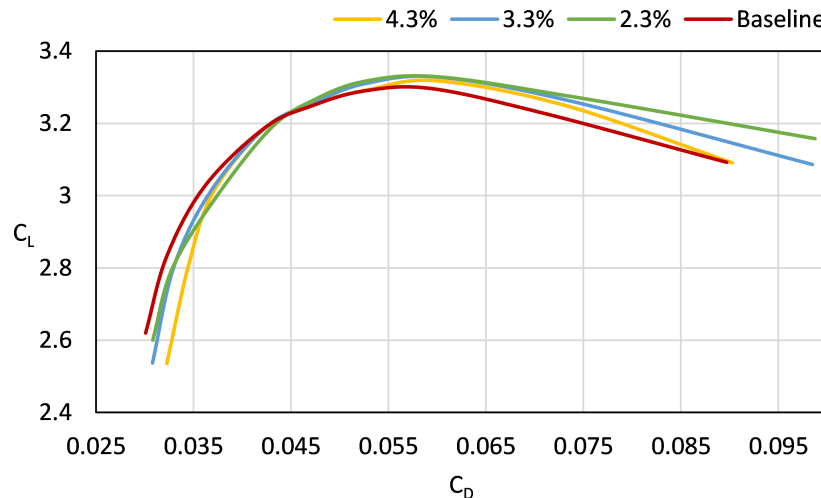
---



(a) Effect of variation of  $x\_gap$  on  $C_L$  vs  $\alpha$ , with  $y\_gap$  fixed at 4.0% of the airfoil chord.



(b) Effect of variation of  $x\_gap$  on  $C_D$  vs  $\alpha$ , with  $y\_gap$  fixed at 4.0% of the airfoil chord.



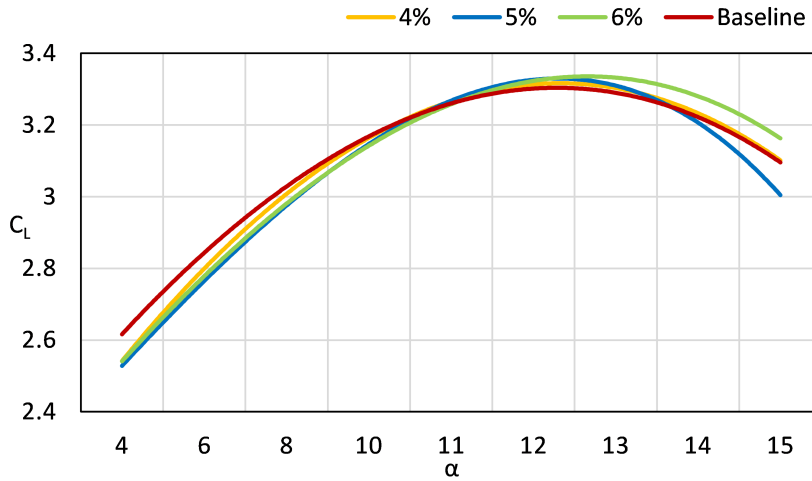
(c) Effect of variation of  $x\_gap$  on  $C_L$  vs  $C_D$ , with  $y\_gap$  fixed at 4.0% of the airfoil chord.

**Figure 3.4:** Aerodynamic performance characteristics ( $C_L$  &  $C_D$ ) as a function of angle of attack ( $\alpha$ ) for varying  $x\_gap$  at a fixed  $y\_gap$  of 4.0% of the airfoil chord.

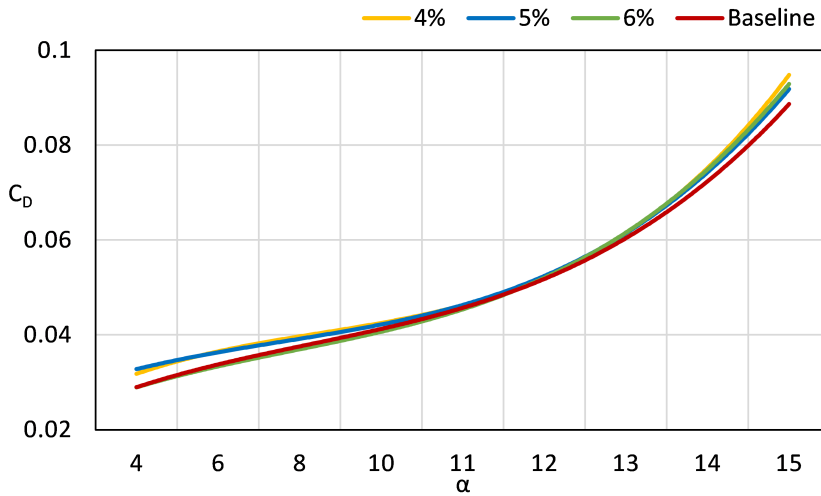
---

### 3 Trade Studies

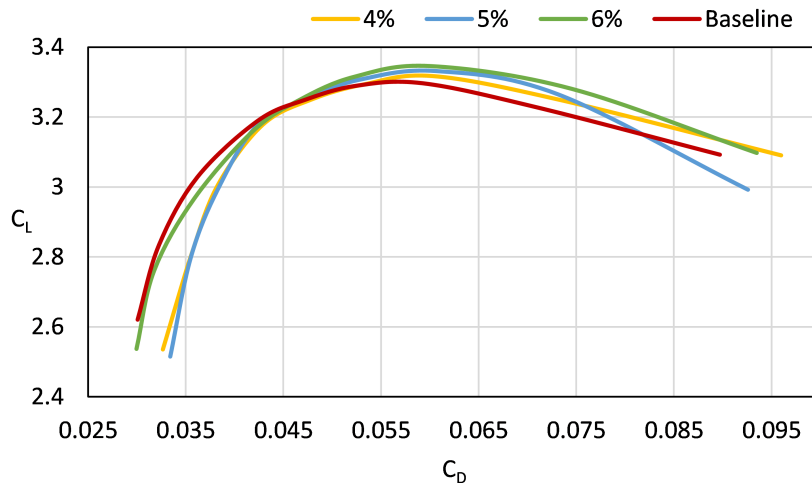
---



(a) Effect of variation of  $y\_gap$  on  $C_L$  vs  $\alpha$ , with  $x\_gap$  fixed at 4.3% of the airfoil chord.



(b) Effect of variation of  $y\_gap$  on  $C_D$  vs  $\alpha$ , with  $x\_gap$  fixed at 4.3% of the airfoil chord.



(c) Effect of variation of  $y\_gap$  on  $C_L$  vs  $C_D$ , with  $x\_gap$  fixed at 4.3% of the airfoil chord

**Figure 3.5:** Aerodynamic performance characteristics ( $C_L$  &  $C_D$ ) as a function of angle of attack ( $\alpha$ ) for varying  $y\_gap$  at a fixed  $x\_gap$  of 4.3% of the airfoil chord.

---



(a) Eddy viscosity contours: Baseline configuration ( $x\_gap$  at 3.0% &  $y\_gap$  at 1.5% of the airfoil chord) at 4-degree AoA and 30-degree flap deflection.

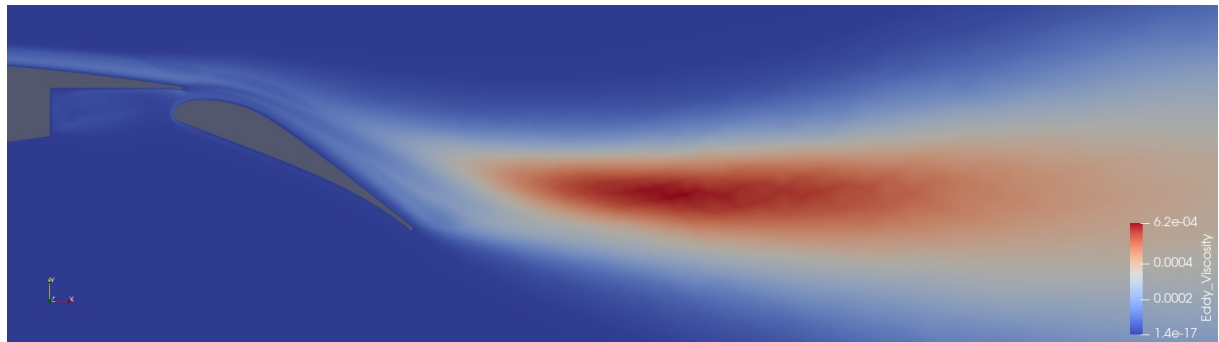


(b) Eddy viscosity contours: Optimized configuration ( $x\_gap$  at 2.3% &  $y\_gap$  at 4.0% of the airfoil chord) at 4-degree AoA and 30-degree flap deflection.

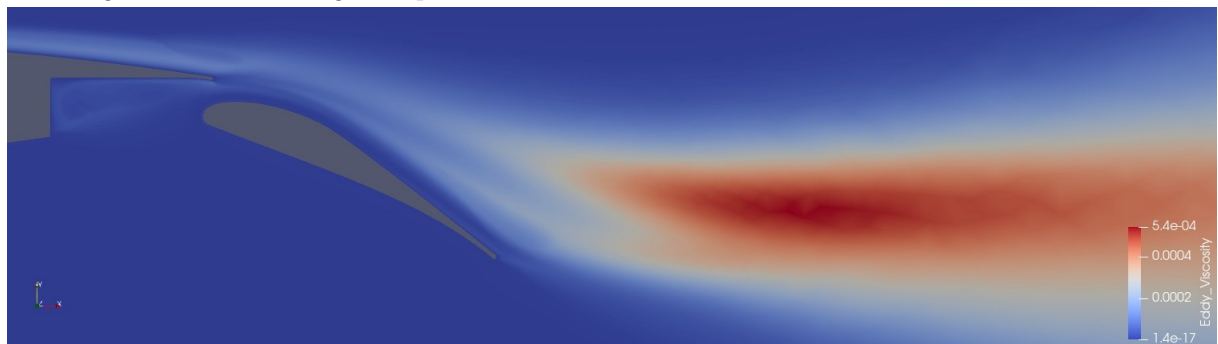


(c) Eddy viscosity contours: Optimized configuration ( $x\_gap$  at 4.3% &  $y\_gap$  at 6.0% of the airfoil chord) at 4-degree AoA and 30-degree flap deflection.

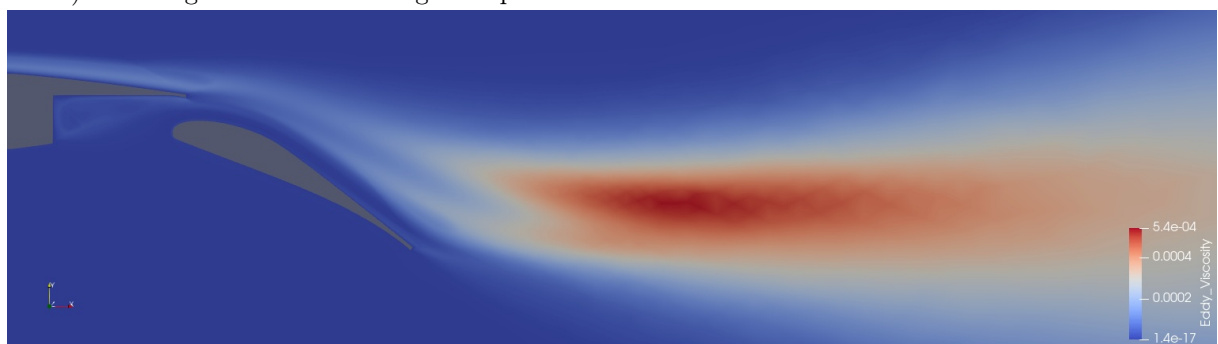
**Figure 3.6:** Eddy viscosity contours: Comparison of baseline and optimized  $x\_gap$  &  $y\_gap$  configurations at 4-degree AoA and 30-degree flap deflection.



(a) Eddy viscosity contours: Baseline configuration ( $x\_gap$  at 3.0% &  $y\_gap$  at 1.5% of the airfoil chord) at 13-degree AoA and 30-degree flap deflection.



(b) Eddy viscosity contours: Optimized configuration ( $x\_gap$  at 2.3% &  $y\_gap$  at 4.0% of the airfoil chord) at 13-degree AoA and 30-degree flap deflection.



(c) Eddy viscosity contours: Optimized configuration ( $x\_gap$  at 4.3% &  $y\_gap$  at 6.0% of the airfoil chord) at 13-degree AoA and 30-degree flap deflection.

**Figure 3.7:** Eddy viscosity contours: Comparison of baseline and optimized  $x\_gap$  &  $y\_gap$  configurations at 13-degree AoA and 30-degree flap deflection.

A detailed analysis of the updated aerodynamic coefficients, presented in Figure 3.8, reveals the improved performance characteristics of the 2.3% *x\_gap* and 6% *y\_gap*. The data demonstrates that this configuration (green line) consistently achieves higher lift coefficients ( $C_L$ ) across the entire range of angles of attack compared to the baseline (red line), as illustrated in Figure 3.8a, resulting in a notable 2.43% increase in maximum lift coefficient ( $C_{L_{max}}$ ). This significant improvement in  $C_{L_{max}}$  indicates a greater capacity for lift generation. While the updated configuration exhibits increased drag, as shown in Figure 3.8b, Figure 3.8c clearly illustrates a more favorable lift-to-drag relationship, particularly in the mid-to-high lift coefficient region. This improved lift-to-drag efficiency showcases the ability of this configuration to generate more lift for a given drag penalty within the performance range.

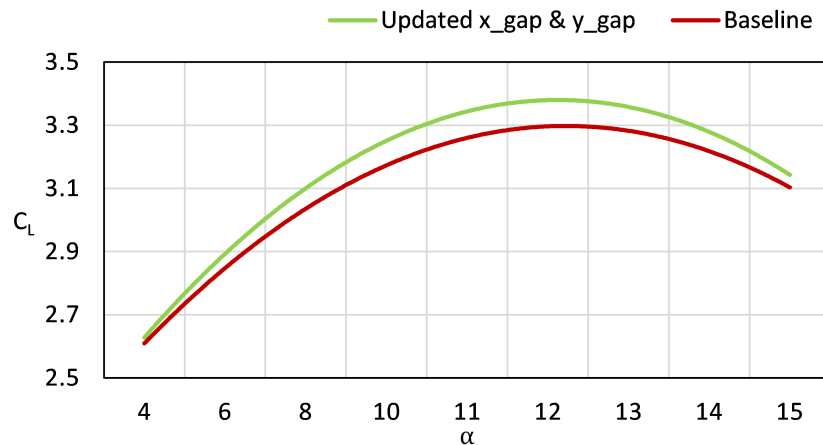
The flow visualization further supports these findings. At a low angle of attack of 4 degrees as illustrated in Figure 3.9, the optimized configuration (Figure 3.9b) shows less turbulent flow exiting the channel and a reduced region of high eddy viscosity over the flap's leading edge compared to the baseline (Figure 3.9a), although some increased turbulence is observed at the flap cutout. This localized turbulence is outweighed by the overall improved flow characteristics. At a higher angle of attack, as shown in Figure 3.10, the optimized configuration (Figure 3.10b) continues to exhibit a less turbulent flow over the flap. This suggests a more energized and attached flow over the flap surface in contrast to the baseline configuration (Figure 3.10a) at 13 degrees AoA.

Across both angles of attack, the eddy viscosity pattern indicates that the optimized design promotes a more favorable flow regime over the flap. The reduced eddy viscosity, particularly near the leading edge suggests a more streamlined flow with less energy dissipation possibly due to reduced turbulence. This flow behavior is in line with the observed improvements in lift and lift-to-drag efficiencies from the plots in Figure 3.8.

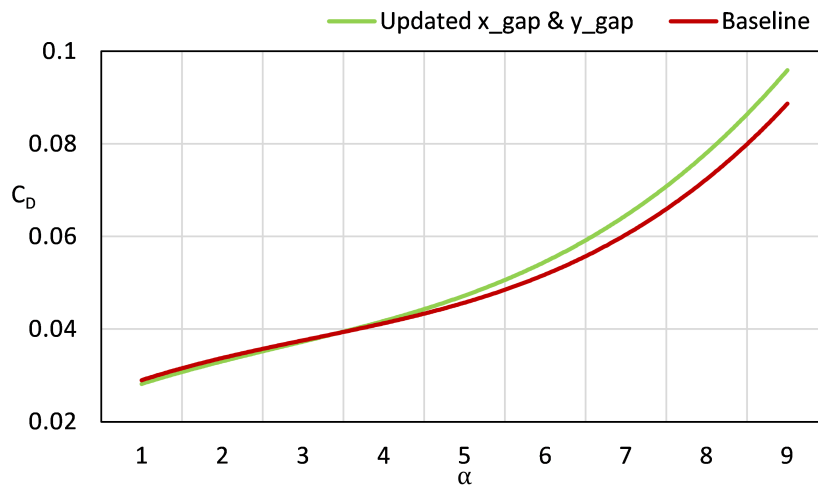
The combined evidence from the updated graphs and flow visualizations support the superior aerodynamic performance of the 2.3% *x\_gap* and 6% *y\_gap* configuration. The enhancements in lift generation, lift-to-drag efficiency (Figure 3.8), and improved flow characteristics over the flap, notable at both 4 degrees (Figure 3.9) and 13 degrees (Figure 3.10) validate the effectiveness of the optimized configuration in enhancing the high-lift performance.

### 3 Trade Studies

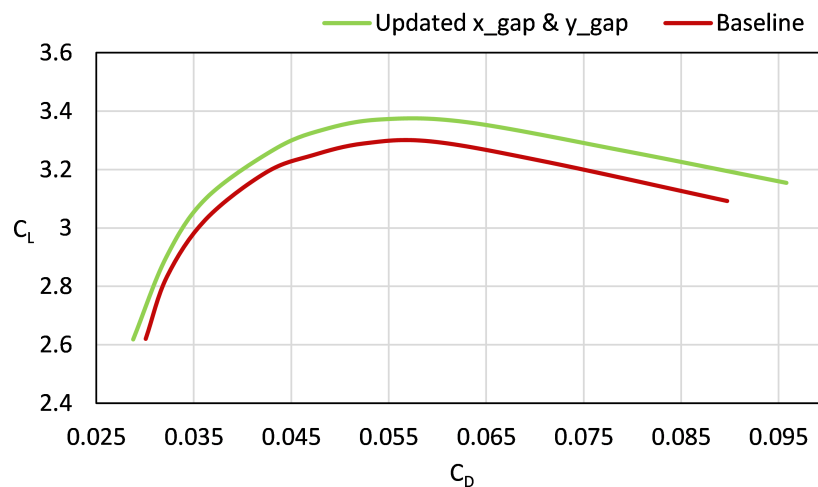
---



(a) Comparison of baseline and updated configuration (x\_gap at 2.3% and y\_gap 6.0%) for  $C_L$  vs  $\alpha$ .

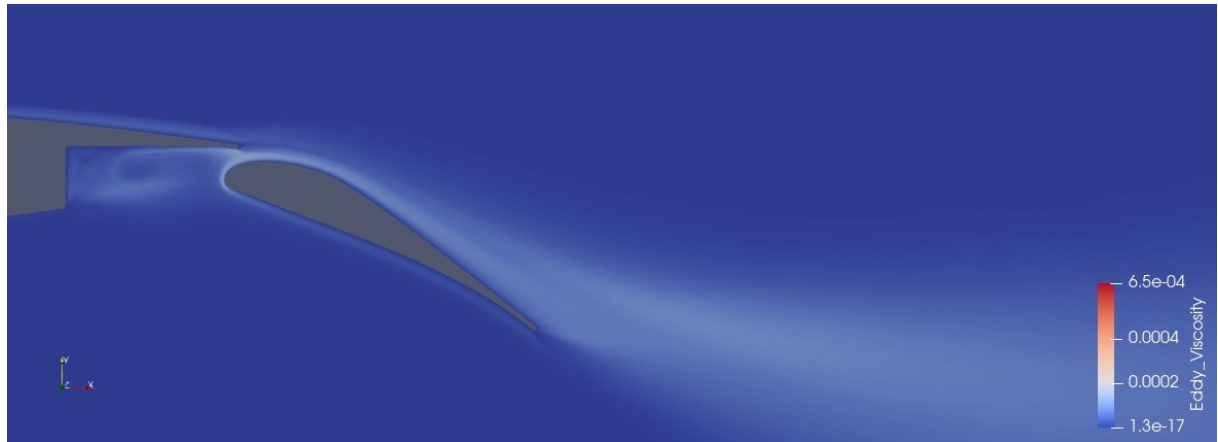


(b) Comparison of baseline and updated configuration (x\_gap at 2.3% and y\_gap 6.0%) for  $C_D$  vs  $\alpha$ .

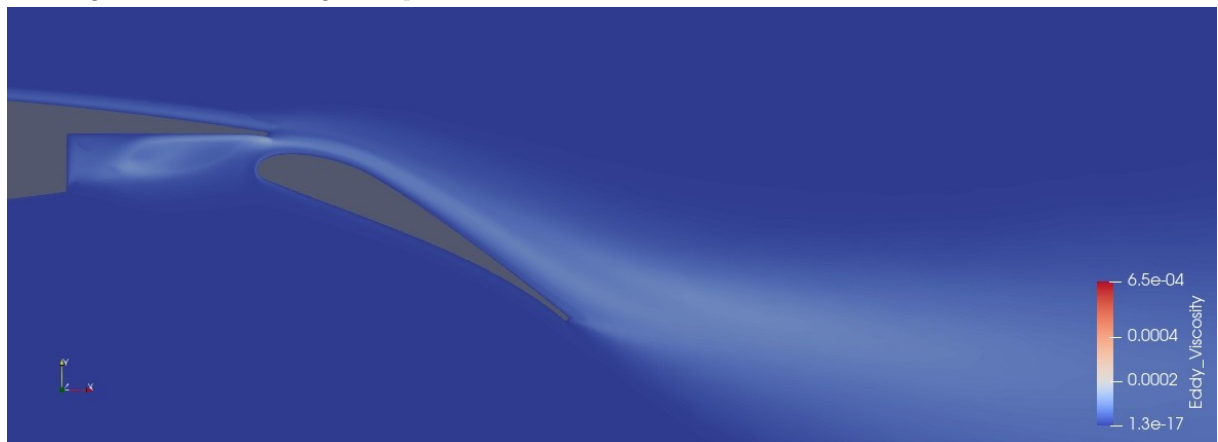


(c) Comparison of baseline and updated configuration (x\_gap at 2.3% and y\_gap 6.0%) for  $C_L$  vs  $C_D$ .

**Figure 3.8:** Comparison of baseline and updated configuration: Aerodynamic performance characteristics ( $C_L$  &  $C_D$ ) as a function of angle of attack ( $\alpha$ )

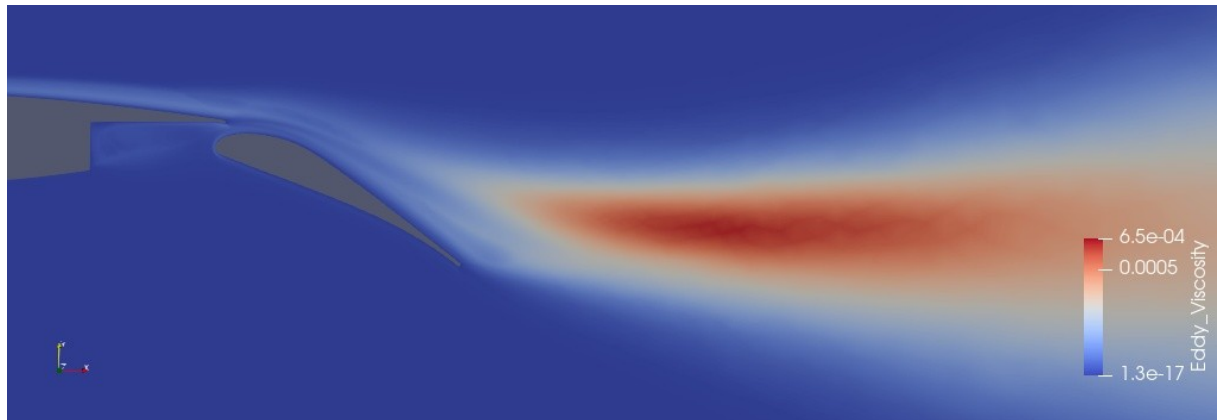


(a) Eddy viscosity contours: Baseline configuration ( $x\_gap$  at 3.0% &  $y\_gap$  at 1.5% of the airfoil chord) at 4-degree AoA and 30-degree flap deflection.

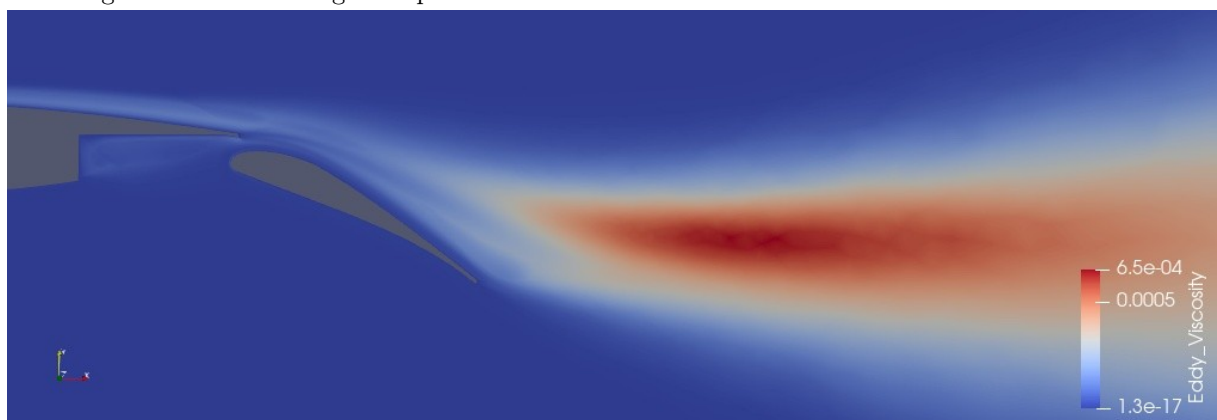


(b) Eddy viscosity contours: Updated configuration ( $x\_gap$  at 2.3% &  $y\_gap$  at 6.0% of the airfoil chord) at 4-degree AoA and 30-degree flap deflection.

**Figure 3.9:** Eddy viscosity contours: Comparison of baseline and updated  $x\_gap$  &  $y\_gap$  configurations at 4-degree AoA and 30-degree flap deflection.



(a) Eddy viscosity contours: Baseline configuration ( $x\_gap$  at 3.0% &  $y\_gap$  at 1.5% of the airfoil chord) at 13-degree AoA and 30-degree flap deflection.



(b) Eddy viscosity contours: Updated configuration ( $x\_gap$  at 2.3% &  $y\_gap$  at 6.0% of the airfoil chord) at 13-degree AoA and 30-degree flap deflection.

**Figure 3.10:** Eddy viscosity contours: Comparison of baseline and updated  $x\_gap$  &  $y\_gap$  configurations at 13-degree AoA and 30-degree flap deflection.

### 3.2 Concluding remarks

In summary, while the initial parameter sensitivity analysis highlighted the `x_gap` and `y_gap` as the parameters with the most significant influence on the aerodynamic coefficients, the overall contribution of other geometric parameters was crucial to the detailed optimization of the Fowler flap. The effects of parameters such as the flap chord ratio, shroud dimensions, lip geometry, and conical shapes, though less pronounced in isolation, played a vital role in achieving the final optimized configuration. The careful calibration of all geometric parameters resulted in a notable enhancement of the overall high-lift performance compared to the initial baseline design.

Having established the influence of individual and combined geometric parameters on the Fowler flap's high-lift performance through this trade study, the next section will detail the aerodynamic improvements achieved with the fully optimized configuration. This section will provide a direct comparison against the baseline design, demonstrating the significant aerodynamic enhancements achieved through this comprehensive optimization process.

## 4 Results

This chapter presents the findings obtained from the Computational Fluid Dynamics (CFD) analysis conducted to evaluate the aerodynamic performance of both the baseline and optimized Fowler flap configurations, designed for an airfoil equipped with a Hybrid Laminar Flow Control (HLFC) system. As outlined in the previous chapter, mesh and parameter studies were conducted at two specific flap deflections and the resulting aerodynamic characteristics of the deflection (30 degrees) with greater response to change in design parameters were compared across a range of angles of attack.

The key aerodynamic parameters assessed include the lift coefficient ( $C_L$ ) and the drag coefficient ( $C_D$ ). Additionally, the flow behavior around the deployed flap was investigated using visualization of eddy viscosity at representative angles of attack (4 degrees and 13 degrees), providing insight into the flow physics and highlighting the influence of the `x_gap` and `y_gap` parameters.

It is important to note that, while this thesis focuses on optimizing the Fowler flap for an HLFC airfoil, the effects of this hybrid laminar flow control were not directly modeled within the aerodynamic analysis. Therefore, the results presented here reflect the isolated aerodynamic performance of the flap configurations and serve as a foundation for understanding their potential interaction with an active HLFC system in future studies.

The following sections present a comparative analysis of the aerodynamic coefficients at both flap deflections (15 and 30 degrees), across an angle of attack sweep from 0 to 15 degrees, showcasing the outcome of the parameter optimization detailed in the previous chapter. Alongside this, the flow field characteristics are analyzed, with the aerodynamic trends further supported by flow visualizations, providing a comprehensive understanding of the flow physics.

### 4.1 Flap design parameters

Table 4.1 presents the key design parameters that define the baseline and the optimized Fowler flap configurations. These parameters are expressed as ratios, either with respect to the airfoil chord (Table 4.1a) or with respect to the flap chord (Table 4.1b). The flap deflection for both configurations was evaluated at 15 and 30 degrees.

Table 4.1a presents parameters scaled by the airfoil chord. Here, we can see that the optimized design features a slightly increased shroud chord ratio (`csr_c` = 0.90 compared to 0.85 for the baseline) and a significantly larger `y_gap` (`y_gap` = 0.0197 compared to 0.005 for the baseline). On the contrary, the `x_gap` is reduced in the optimized design (`x_gap` = 0.0075 compared to 0.01 for the baseline). The flap chord ratio (`cf_c`) and shroud tip thickness (`tc_shr_tip`) remain unchanged between the two configurations.

Table 4.1b presents parameters defined with respect to the flap chord. Here, the optimized design exhibits a larger conical curve extent ratio (`ce_c` = 0.375 compared to

0.3) and a larger flap leading edge radius ( $r_{le\_flap} = 0.0135$  compared to 0.01). The conical parameter ( $w_{conic}$ ) is also increased in the optimized design (0.75 compared to 0.5) while the shroud lip extent ratio ( $clip\_ext$ ) remains the same. These changes in geometric parameters in the optimized design influence the flow behavior around the flap and consequently the overall aerodynamic performance.

**Table 4.1:** Baseline and optimized flap design parameters (in ratios).

(a) Parameters defined with respect to the airfoil chord.

Parameter	Notation	Baseline	Optimized
Flap chord ratio	$cf_c$	0.3	0.3
Shroud tip thickness	$tc_{shr\_tip}$	0.003	0.003
Shroud chord ratio	$csr_c$	0.85	0.90
X-Gap	$x_{gap}$	0.01	0.0075
Y-Gap	$y_{gap}$	0.005	0.0197

(b) Parameters defined with respect to the flap chord.

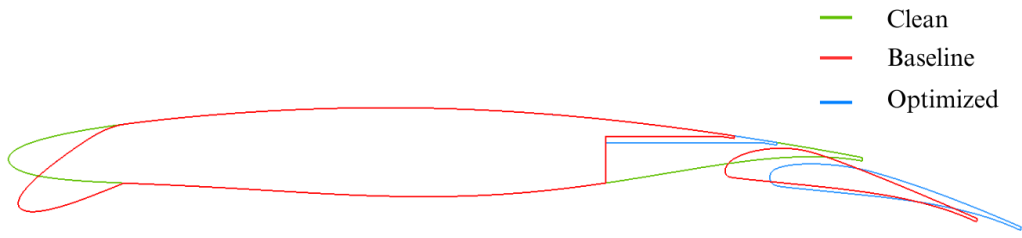
Parameter	Notation	Baseline	Optimized
Shroud lip extent ratio	$clip_{ext}$	0.05	0.05
Conical curve extent ratio	$ce_c$	0.3	0.375
Flap leading edge radius	$r_{le\_flap}$	0.01	0.0135
Conical parameter	$w_{conic}$	0.5	0.75
Flap deflection	$\delta_f$	15°, 30°	15°, 30°

Figure 4.1 provides a visual comparison of the baseline and optimized flap configurations. In Figure 4.1a, both designs are shown at a flap deflection of 15 degrees - red for the baseline and blue for the optimized - alongside the clean airfoil (green) for reference. The reshaped shroud shape and the increased  $y_{gap}$  in the optimized design are visible.

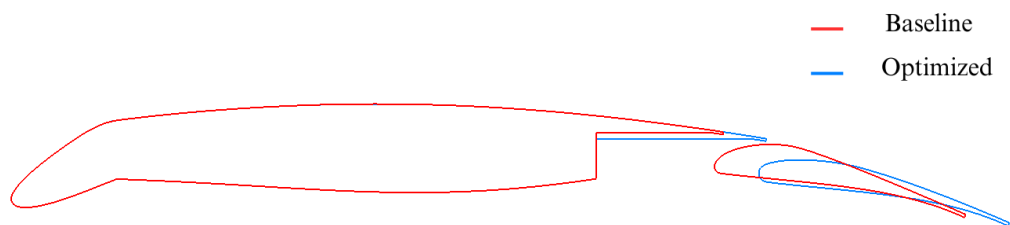
Figure 4.1b gives a closer look at just the baseline and optimized designs at 15-degree flap deflection, helping highlight subtle differences in the leading-edge radius, flap curvature, and shroud geometry.

Similarly, Figure 4.1c compares the baseline and the optimized design at 30-degree flap deflection. The increased deflection highlights the deployed position of the optimized configuration relative to the baseline and also the larger vertical distance created by the  $y_{gap}$ .

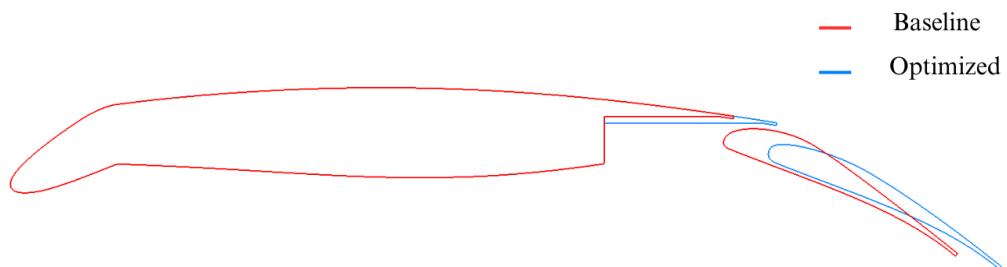
Finally, Figure 4.1d shows the isolated flap design, offering another angle to observe the geometric differences. Here, the leading and trailing edge points are intentionally overlapped to align the configurations at key reference positions, making it easier to compare.



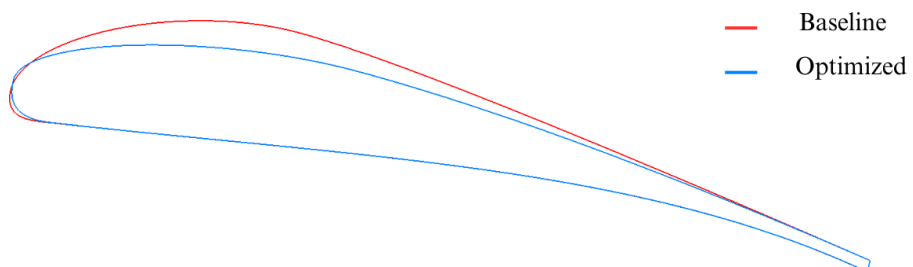
(a) Clean, baseline and optimized airfoil and flap designs at 15-degree flap deflection.



(b) Baseline and optimized airfoil and flap designs at 15-degree flap deflection.



(c) Baseline and optimized airfoil and flap designs at 30-degree flap deflection.



(d) Baseline and optimized flap designs.

**Figure 4.1:** Comparison of baseline and optimized airfoil and flap geometric profiles (all parameters optimized).

## 4.2 Aerodynamic performance at 15-degree flap deflection

Figure 4.2 presents the aerodynamic coefficients for the baseline (red) and optimized (blue) configurations at a 15-degree flap deflection.

- **Lift Coefficient ( $C_L$ ) vs Angle of Attack ( $\alpha$ )** (Figure 4.2a):

Initially, both configurations exhibit a similar linear increase in  $C_L$  with  $\alpha$ . However, beyond approximately 6 degrees angle of attack, the optimized design starts to generate noticeably higher lift. The maximum lift coefficient ( $C_{L_{\max}}$ ) achieved by the optimized design is 3.02, which is visibly higher than the baseline's  $C_{L_{\max}}$  of 2.90, an increase of 4.14%.

- **Lift Coefficient ( $C_L$ ) vs Drag Coefficient ( $C_D$ )** (Figure 4.2b):

The plot reveals that for a given lift coefficient, particularly in the range above  $C_L \approx 1.8$ , the optimized design exhibits an improved performance as it achieves a higher  $C_{L_{\max}}$ , at the expense of increased drag. Despite this higher absolute drag at maximum lift, the optimized design exhibits a favorable  $C_L$  vs  $C_D$  relationship in the high-lift regime.

- **Lift-to-Drag Ratio ( $L/D$ ) vs Angle of Attack ( $\alpha$ )** (Figure 4.2c):

At lower angles of attack ( $\alpha \approx 8$  degrees), the optimized design demonstrates slightly higher  $L/D$  with a peak value of approximately 101.81 at  $\approx 8$  degrees, compared to the baseline's peak  $L/D$  value of 97.23 at  $\approx 8$  degrees. This suggests improved aerodynamic efficiency in the low to moderate lift regimes. While the  $L/D$  values converge at higher angles of attack, the optimized design is still generating more absolute lift at these points (as seen in Figure 4.2a).

In combination with the representation of the aerodynamic coefficients in their respective plots, the flow visualization provides crucial insights into the reasons behind the differences in aerodynamic performances.

- **At a low Angle of Attack ( $\alpha = 4$  degrees):**

Examining the Turbulent Kinetic Energy (TKE) in Figure 4.3, a distinct difference in the flow around the flap and the shroud can be observed. For the baseline configuration (Figure 4.3a), the TKE within the flap cutout region is low. However, there are higher TKE values concentrated at the leading edge and along the upper surface of the flap. This localized increase in turbulence could be linked to the smaller  $y\_gap$ , leading to a stronger interaction between the recirculation flow within the flap cutout and the flap's leading edge and also due to the disturbed channel flow which likely interacts with the flow exiting the airfoil near the shroud, causing turbulent flow interaction along the upper surface of the flap.

This interaction is further supported by the Eddy Viscosity contours in Figure 4.5. The baseline (Figure 4.5a) shows that the flap's leading edge is situated within the region of higher eddy viscosity, indicating the influence of recirculation flow from the cutout. The reduced  $y\_gap$  and the flap profile also seem to push the channel

flow upwards and into the shear layers from the flow of the main airfoil exiting above the shroud, potentially increasing the local turbulence.

In contrast, the optimized configuration (Figure 4.3b) exhibits higher TKE within the flap cutout itself, but significantly lower TKE at the flap's leading edge and upper surface. This suggests that the increased  $y_{gap}$  and modified shroud chord ratio  $csr_c$  in the optimized design has effectively moved the flap out of the primary influence zone of the recirculation within the cutout, resulting in a comparatively less turbulent flow through the lower sections of the channel, over the flap's leading edge and upper surface. This is also evident in the lower eddy viscosity levels observed in Figure 4.5b around the optimized flap, including the pressure side.

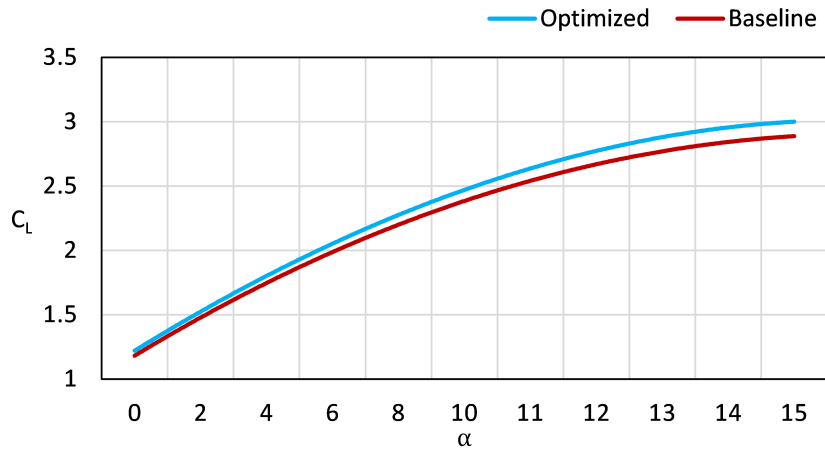
However, the increased shroud chord ratio ( $csr_c$ ) in the optimized might have possibly intensified the recirculation within the flap cutout, leading to a higher TKE in that region. Furthermore, Figure 4.5b indicates a stronger interaction between the enhanced circulation and the shroud tip in the optimized design, showcasing a slightly higher eddy viscosity near the tip.

- **At a higher Angle of Attack ( $\alpha = 15$  degrees):**

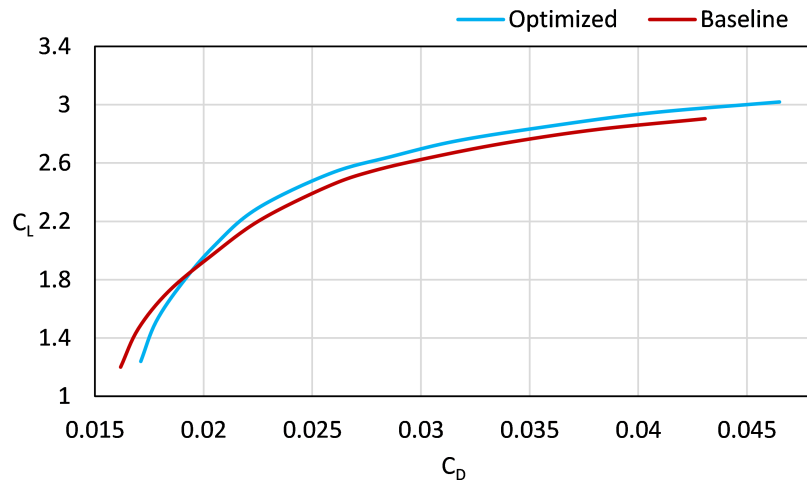
In Figure 4.4(TKE) and Figure 4.6 (Eddy Viscosity), the benefits of the optimized geometry becomes more apparent regarding the flow separation above the flap. The baseline configuration exhibits a noticeable region of TKE (Figure 4.4a) and a large region of high eddy viscosity (Figure 4.6a) along the upper surface of the flap, signifying extensive and energetic flow separation.

The optimized design demonstrates a significant reduction in the extent and intensity of this separated flow. The TKE (Figure 4.4b) and eddy viscosity contours (Figure 4.6b) over the optimized flap are comparatively less widespread closer along the upper surface, indicating a more attached flow.

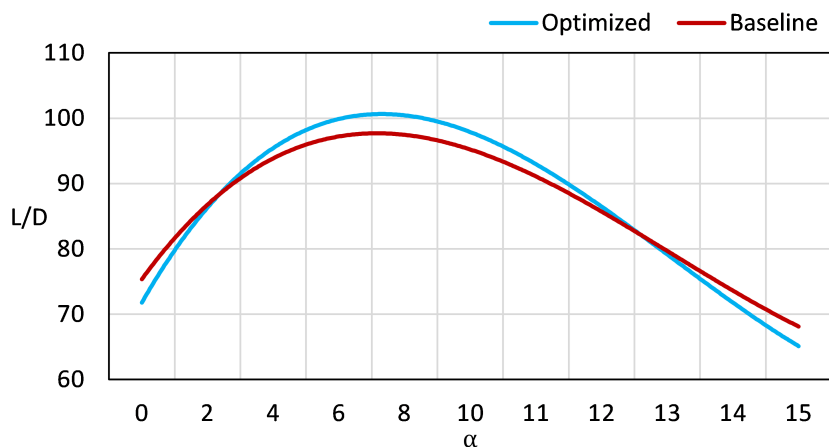
While the local flow over the optimized flap is cleaner compared to the baseline, Figure 4.6b representing the Eddy Viscosity at 15 degrees angle of attack suggests that the wake behind the optimized flap is wider and exhibits a core with higher eddy viscosity compared to the baseline. This is also visible in the Figure 4.2c, wherein the  $L/D$  vs  $\alpha$  plot showcases that the optimized design shows a weaker performance as it crosses an angle of attack of approximately  $\alpha \approx 12$  degrees. This could be the trade-off resulting from the altered interaction between the flap, shroud, and the channel flow exiting the flap cutout, potentially increasing the overall drag at these higher angles of attack despite the improved flow over the flap's upper surface.



(a) Comparison of baseline and optimized configuration for  $C_L$  vs  $\alpha$  (15-degree flap deflection).

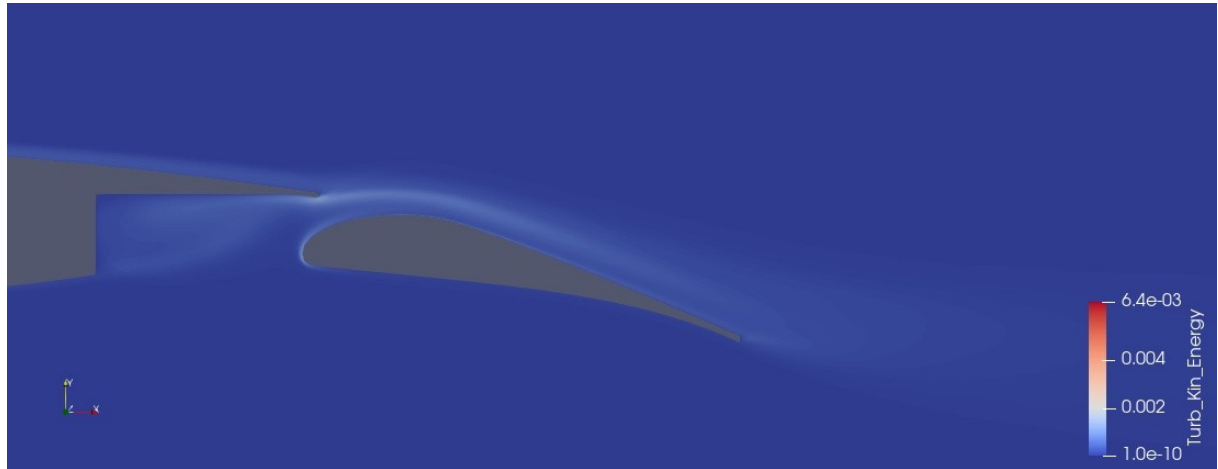


(b) Comparison of baseline and optimized configuration for  $C_L$  vs  $C_D$  (15-degree flap deflection).

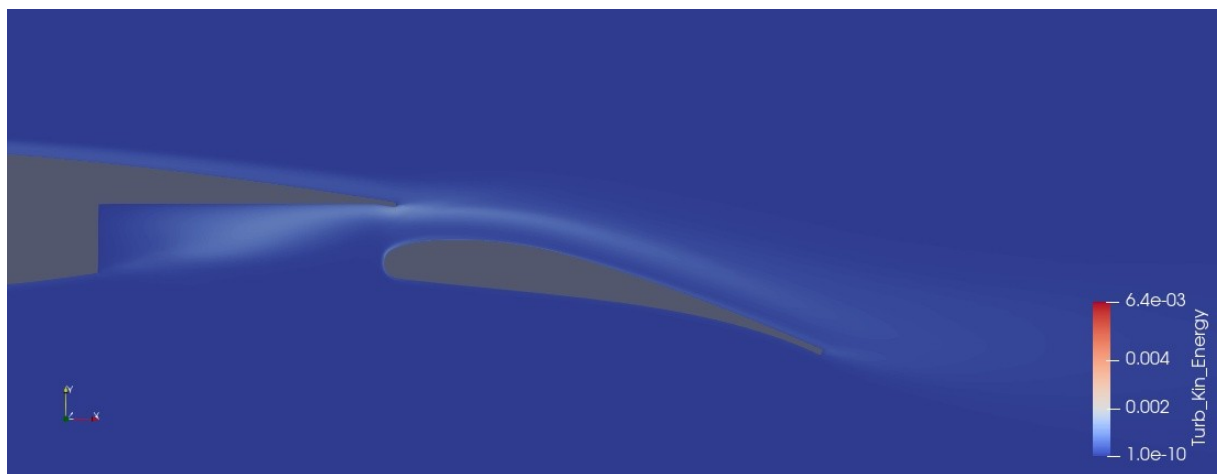


(c) Comparison of baseline and optimized configuration for  $L/D$  vs  $\alpha$  (15-degree flap deflection).

**Figure 4.2:** Comparison of baseline and optimized aerodynamic performance for the 15-degree flap deflection configuration (all parameters optimized).

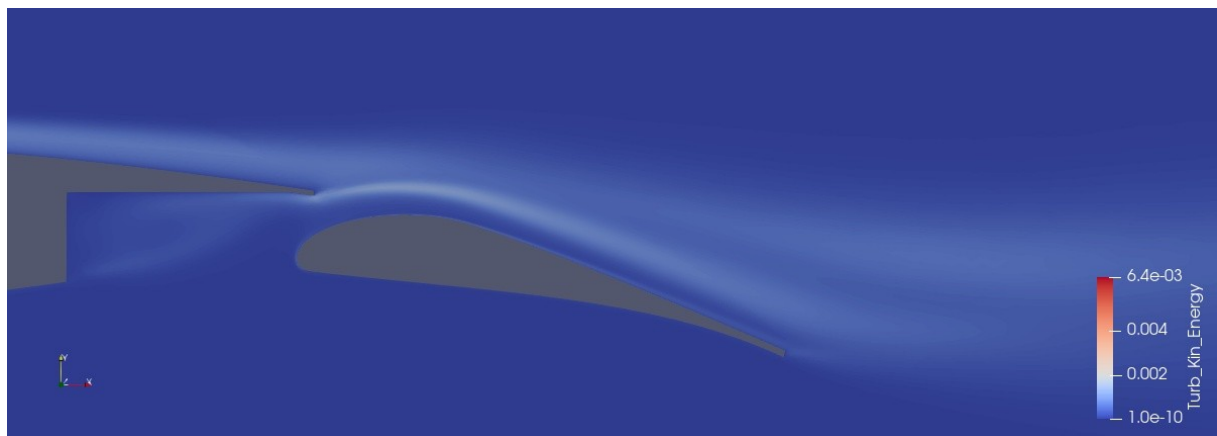


(a) Turbulent kinetic energy contours: Baseline configuration at 4-degree AoA and 15-degree flap deflection.

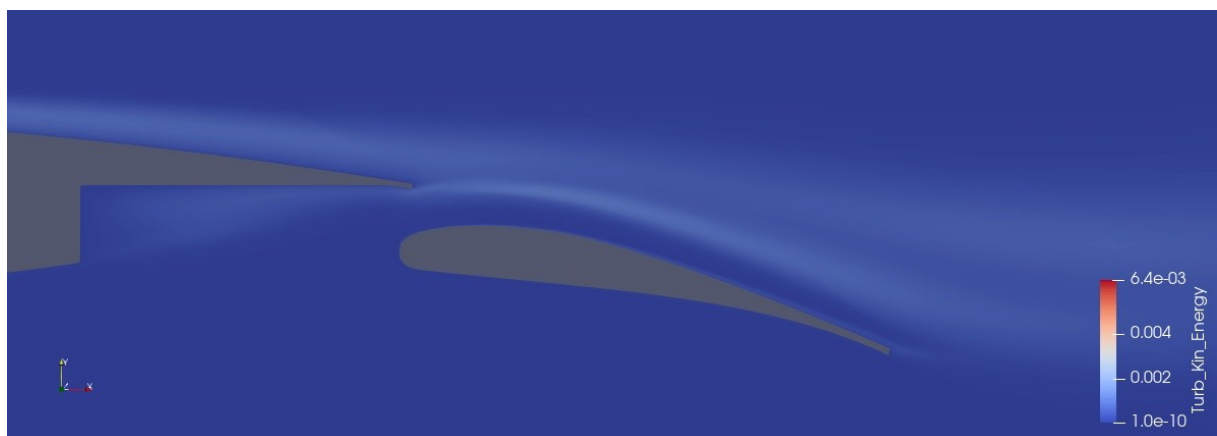


(b) Turbulent kinetic energy contours: Optimized configuration at 4-degree AoA and 15-degree flap deflection.

**Figure 4.3:** Turbulent kinetic energy contours: Comparison of baseline and optimized configurations at 4-degree AoA and 15-degree flap deflection.

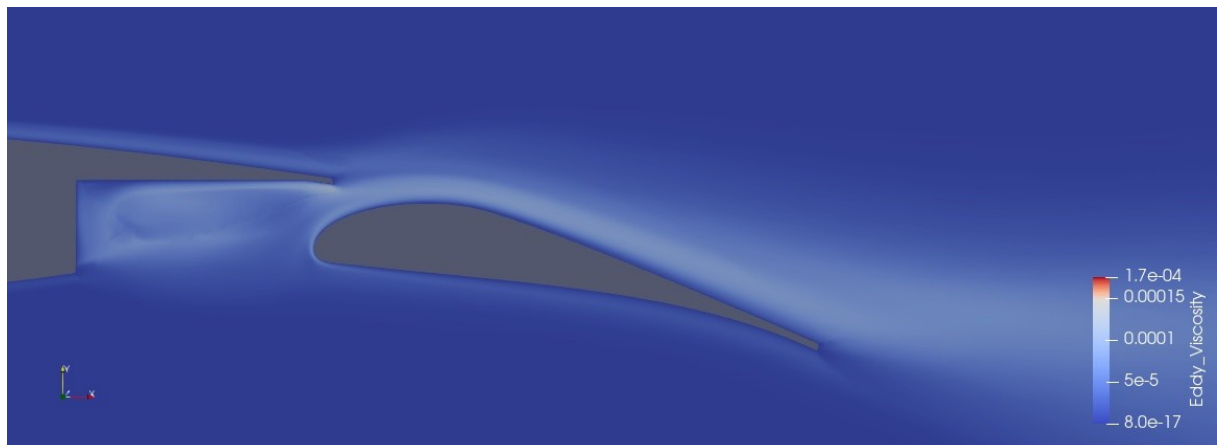


(a) Turbulent kinetic energy contours: Baseline configuration at 15-degree AoA and 15-degree flap deflection.

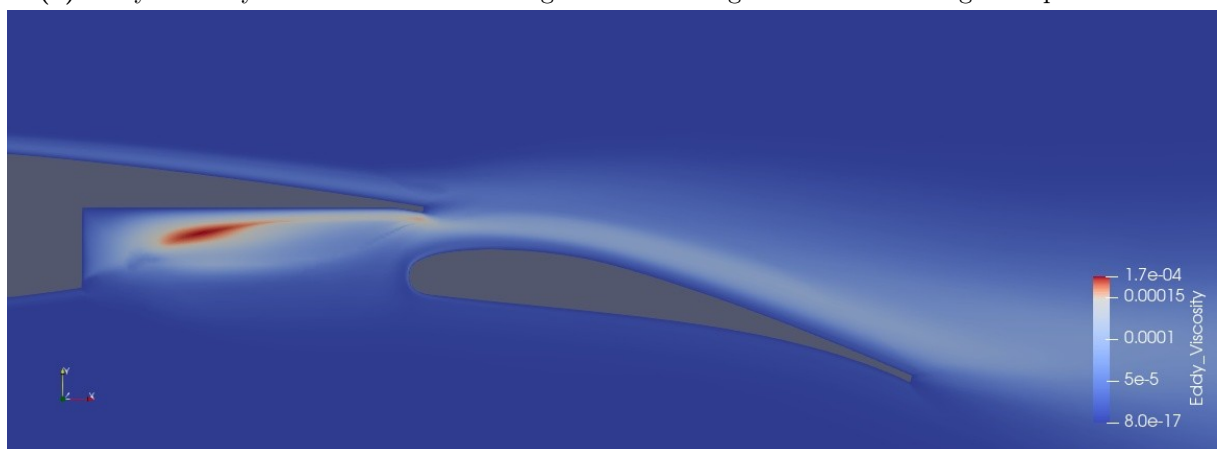


(b) Turbulent kinetic energy contours: Optimized configuration at 15-degree AoA and 15-degree flap deflection.

**Figure 4.4:** Turbulent kinetic energy contours: Comparison of baseline and optimized configurations at 15-degree AoA and 15-degree flap deflection.



(a) Eddy viscosity contours: Baseline configuration at 4-degree AoA and 15-degree flap deflection.

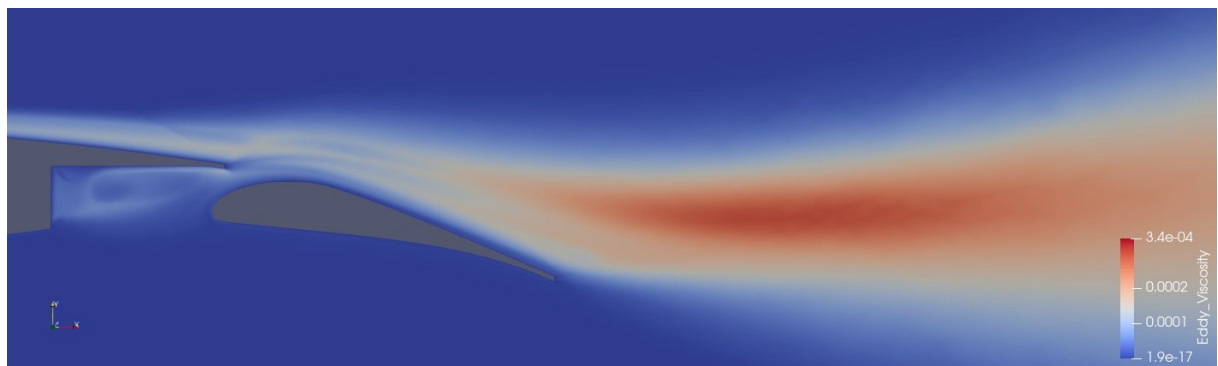


(b) Eddy viscosity contours: Optimized configuration at 4-degree AoA and 15-degree flap deflection.

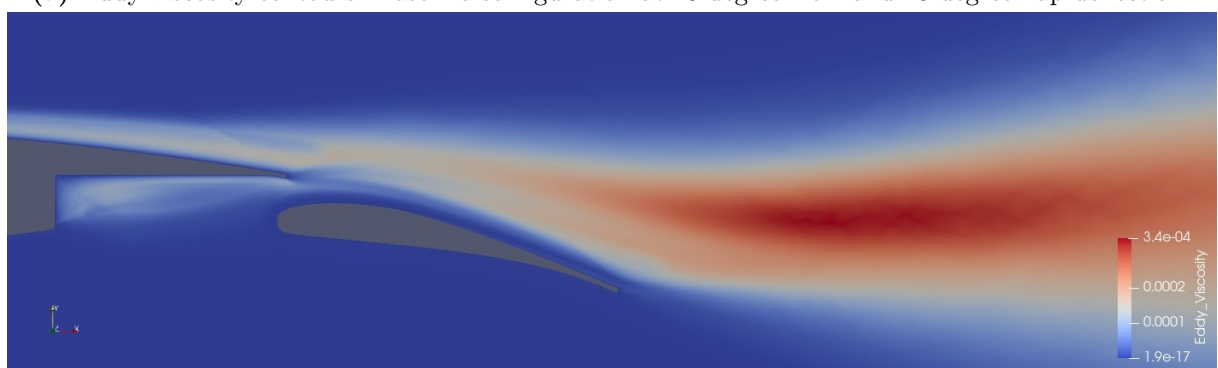
**Figure 4.5:** Eddy viscosity contours: Comparison of baseline and optimized configurations at 4-degree AoA and 15-degree flap deflection.

## 4 Results

---



(a) Eddy viscosity contours: Baseline configuration at 15-degree AoA and 15-degree flap deflection.



(b) Eddy viscosity contours: Optimized configuration at 15-degree AoA and 15-degree flap deflection.

**Figure 4.6:** Eddy viscosity contours: Comparison of baseline and optimized configurations at 15-degree AoA and 15-degree flap deflection.

### 4.3 Aerodynamic performance at 30-degree flap deflection

Figure 4.7 presents the aerodynamic coefficients for the baseline (red) and optimized (blue) configurations at a 30-degree flap deflection.

- **Lift Coefficient ( $C_L$ ) vs Angle of Attack ( $\alpha$ ) (Figure 4.7a):**

Both the baseline (red) and the optimized (blue) designs at a 30-degree flap deflection exhibit a relatively linear increase in  $C_L$  with  $\alpha$  at lower angles. However, beyond approximately 6-8 degrees angle of attack, the increase becomes more nonlinear, possibly due to a gradual increase in flow separation and complex flow behaviors as a consequence. The optimized design stands out by achieving a significantly higher  $C_{L_{\max}}$ . The peak  $C_L$  for the optimized configuration is approximately 3.44, in comparison with the baseline achieving a  $C_{L_{\max}}$  of 3.29. This represents an increase in  $C_{L_{\max}}$  of approximately 4.56% for the optimized design. Furthermore, across the entire tested angle of attack range (0 to 15 degrees), the optimized design consistently generates noticeably higher lift compared to the baseline.

- **Lift Coefficient ( $C_L$ ) vs Drag Coefficient ( $C_D$ ) (Figure 4.7b):**

The plot reveals that to achieve higher lift coefficients, the optimized design (blue) generally operates at a higher drag coefficient compared to the baseline (red). While the optimized configuration reaches a significantly higher  $C_{L_{\max}}$  than the baseline, this enhanced lift capability comes with an increased drag. However, the  $C_L$  vs  $C_D$  relationship indicates that the optimized design can achieve considerably greater lift than the baseline before experiencing a substantial increase in drag, as can be seen between the mid to high  $C_L$  range. The trade-off appears to be that while the optimized design can achieve much higher lift, it does so with a higher overall drag in that high-lift regime.

- **Lift-to-Drag Ratio ( $L/D$ ) vs Angle of Attack ( $\alpha$ ) (Figure 4.7c):**

At lower angles of attack (below  $\alpha \approx 8$  degrees), the optimized configuration exhibits a noticeable superior aerodynamic efficiency, achieving a peak  $L/D$  of approximately 95.58 at around  $\alpha \approx 4$  degrees. This contrasts with the baseline, which attains a maximum  $L/D$  of approximately 87.83 at a slightly higher angle of attack of  $\alpha \approx 6$  degrees, though the optimized still generated a higher  $L/D$  of approximately 90.68 at the same angle of attack. However, beyond  $\alpha \approx 8$  degrees, the  $L/D$  of the optimized design becomes less favorable than the baseline, indicating lower efficiency in generating lift relative to drag at these higher angles. It is important to note that despite this decline in  $L/D$  at higher angles, the optimized design continues to produce a greater absolute lift coefficient compared to the baseline (as illustrated in Figure 4.7a)

In combination with the representation of the aerodynamic coefficients in their respective plots, the flow visualization provides crucial insights into the reasons behind the differences in aerodynamic performances.

- **At a low Angle of Attack ( $\alpha = 4$  degrees):**

Examining the Turbulent Kinetic Energy (TKE) in Figure 4.8, we can observe differences in the turbulent flow structures between the baseline (Figure 4.8a) and optimized (Figure 4.8b) configuration. Similar to the 15-degree flap deflection case, the baseline exhibits a region of low TKE within the flap cutout, but shows a higher TKE concentration originating from the leading edge and along the upper surface of the flap. This can be linked to the interaction of the recirculation flow within the flap cutout with the flow over the flap's leading edge, reduced *y\_gap*, as well as potential disturbances from the channel flow interacting with the flow from main airfoil exiting from over the shroud.

The Eddy Viscosity contours in Figure 4.10 further support this observation. The baseline (Figure 4.10a) shows higher eddy viscosity levels around the flap's leading edge, indicating the influence of the cutout recirculation. The flow exiting above the shroud also appears to interact with the flow over the flap, potentially contributing to increased turbulence along the upper surface.

In contrast, the optimized configuration (Figure 4.8b) displays a higher TKE within the flap cutout region but reduced TKE at the flap's leading edge, and upper surface. This suggests that the increased *y\_gap* and the modified shroud geometry in the optimized design have played a crucial role in moving the flap away from the intense parts of the flow recirculation, leading to a less turbulent flow over the flap's leading edge and the upper surface. This relatively cleaner flow is also visible in the lower eddy viscosity levels around the optimized flap (Figure 4.10b), including both the pressure and suction sides.

However, consistent with the 15-degree case, the increased shroud chord ratio (*csr\_c*) in the optimized design might be contributing to the higher TKE observed within the flap cutout. Additionally, Figure 4.10b showcases a more prominent interaction between the recirculation in the flap cutout, channel flow, and the shroud tip in the optimized design, indicated by a region of higher eddy viscosity near the shroud tip.

- **At a higher Angle of Attack ( $\alpha = 13$  degrees):**

Figure 4.9 presents the Turbulent Kinetic Energy (TKE) contours for the baseline (Figure 4.9a) and optimized (Figure 4.9b) configurations at a 30-degree flap deflection and an angle of attack near the maximum lift (13-degrees). Both configurations exhibit significant regions of TKE originating from the upper surface of the deployed flap, indicating substantial flow separation at this high-lift condition.

However, comparing the two, the optimized design (Figure 4.9b) appears to show a region of high TKE slightly less extensive and potentially less intense along the upper surface of the flap compared to the baseline (Figure 4.9a). The core of the high turbulence region seems to be lifted slightly further from the flap surface in the optimized case. This suggests that while flow separation is significant in both, the optimized design might be managing to control the flow separation to a slightly better extent, which might be leading to a potential higher  $C_{L_{max}}$  as observed in Figure 4.7a.

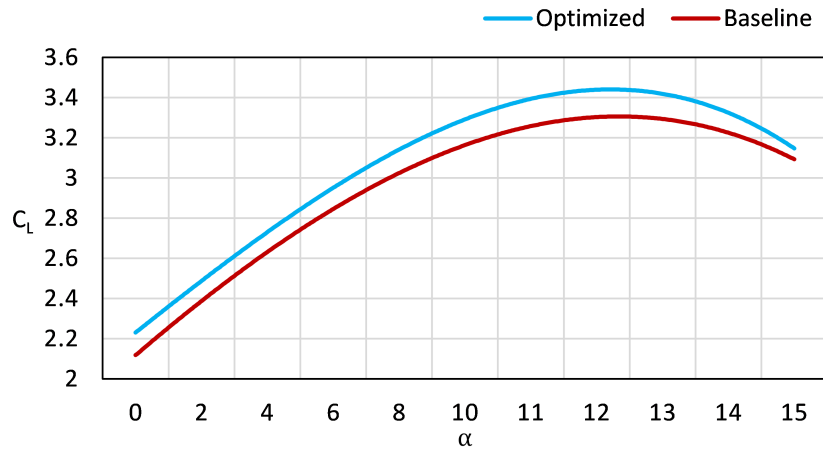
The Eddy Viscosity contours in Figure 4.11 provide further insights into the separated flow. The baseline (Figure 4.11a) shows a large and well-developed region of high eddy viscosity along the region close to the upper surface of the flap, extending from the flap's trailing edge and into the wake, indicating strong and turbulent shear layers. In contrast, the optimized configuration (Figure 4.11b), while still exhibiting substantial high eddy viscosity, reveals a region with a less defined structure and a tendency to remain closer to the flap's upper surface near the trailing edge. This points towards a potentially different pattern of flow separation compared to the more extensive and energetic separation seen in the baseline at this high angle of attack.

The reduced extent and intensity of the high TKE and eddy viscosity regions over the optimized flap at this high angle of attack correlate well with its higher  $C_{L_{max}}$  compared to the baseline. By managing the flow separation more effectively, the optimized design is able to maintain a higher lift force at these critical angles. However, considering the higher TKE at the flap cutout and the interaction of the channel flow with the shroud tip, the flow could potentially have been disturbed as indicated by the high TKE originating from the shroud tip in Figure 4.9a, which might be contributing to a broader, more turbulent wake with an energetic core downstream of the optimized configuration (Figure 4.11b), potentially impacting the drag at higher angles of attack (as illustrated by the  $L/D$  plot in Figure 4.7c)

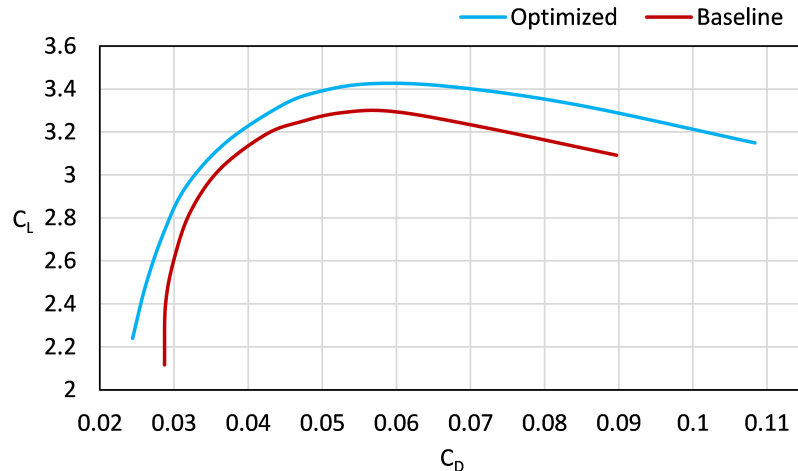
The elevated TKE and Eddy viscosity levels observed at  $\alpha = 4 \& 13$ -degrees with a 30-degree flap deflection, compared to the 15-degree case results from the significant change in the flow field around the deployed flap. This is potentially due to the increased pressure side surface area causing greater flow deflection, coupled with the more pronounced curvature the flow must follow as it accelerates over the suction side.

## 4 Results

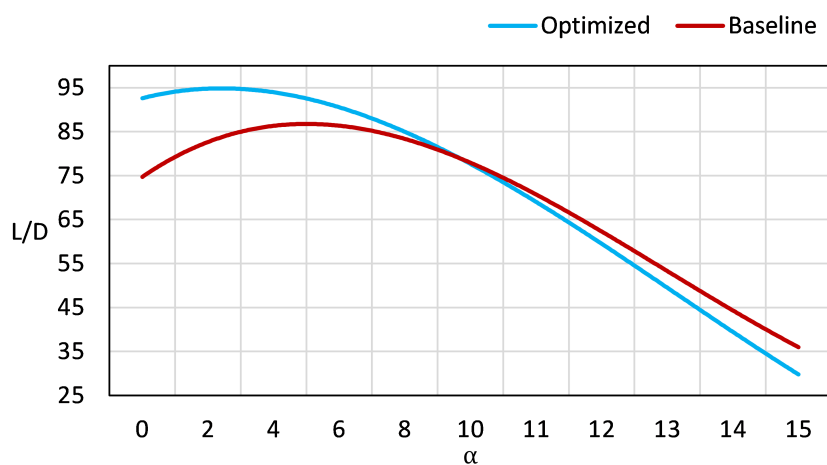
---



(a) Comparison of baseline and optimized configuration for  $C_L$  vs  $\alpha$  (30-degree flap deflection).

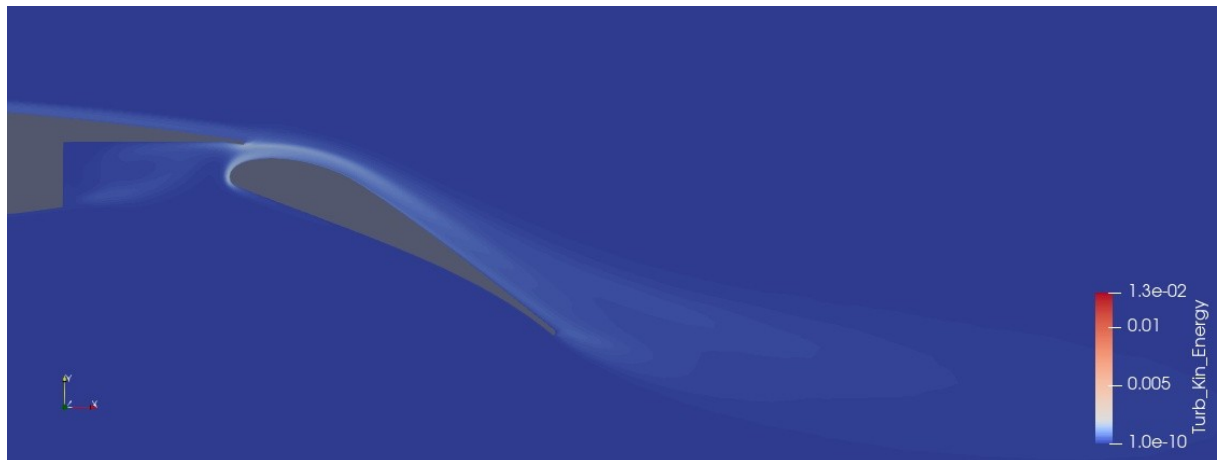


(b) Comparison of baseline and optimized configuration for  $C_L$  vs  $C_D$  (30-degree flap deflection).

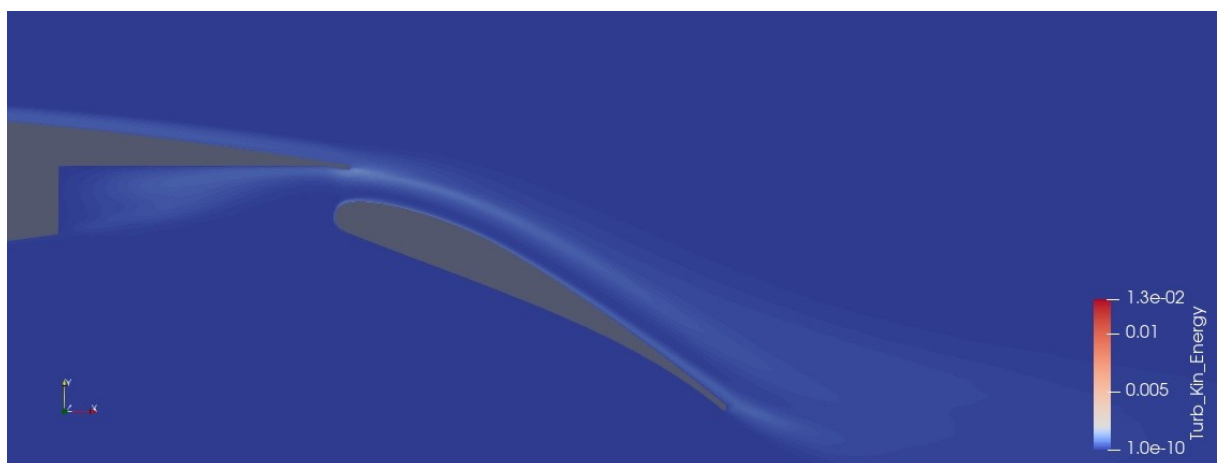


(c) Comparison of baseline and optimized configuration for  $L/D$  vs  $\alpha$  (30-degree flap deflection).

**Figure 4.7:** Comparison of baseline and optimized aerodynamic performance for the 30-degree flap deflection configuration (all parameters optimized)

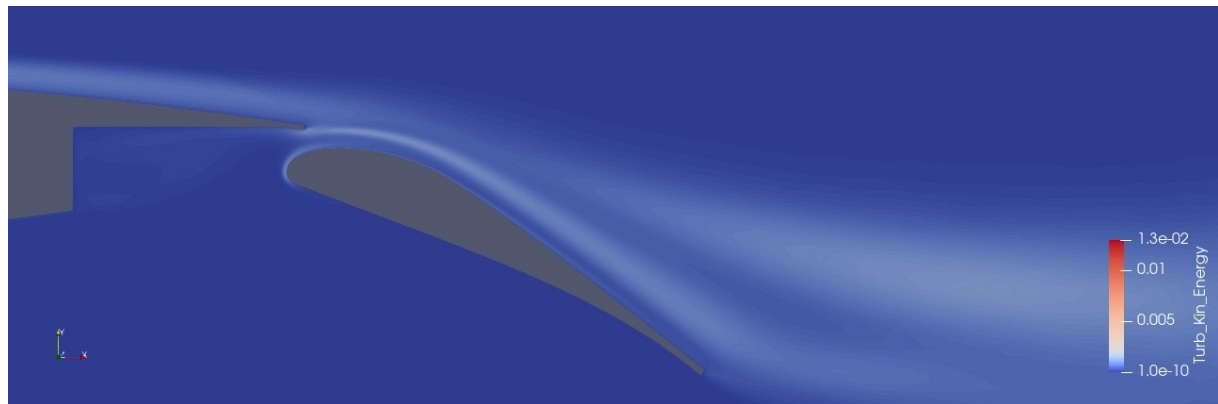


(a) Turbulent kinetic energy contours: Baseline configuration at 4-degree AoA and 30-degree flap deflection.

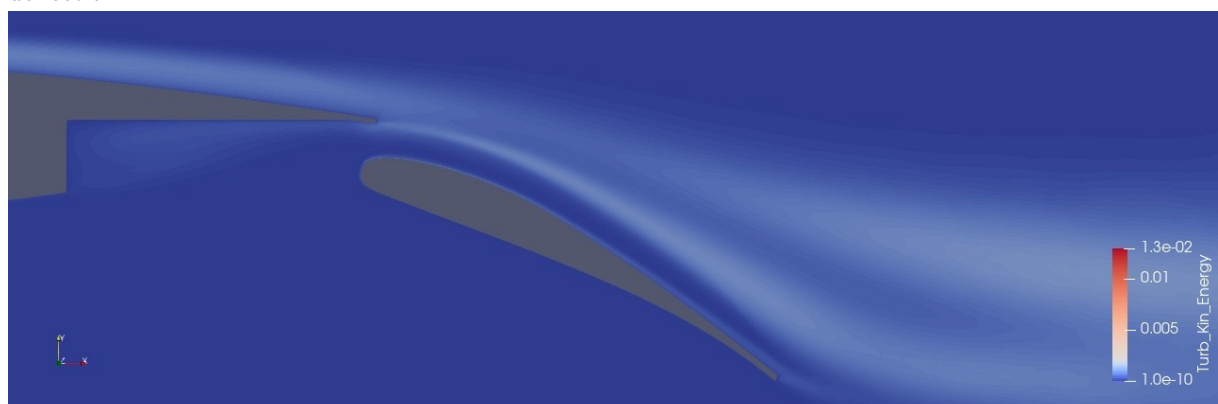


(b) Turbulent kinetic energy contours: Optimized configuration at 4-degree AoA and 30-degree flap deflection.

**Figure 4.8:** Turbulent kinetic energy contours: Comparison of baseline and optimized configurations at 4-degree AoA and 30-degree flap deflection.

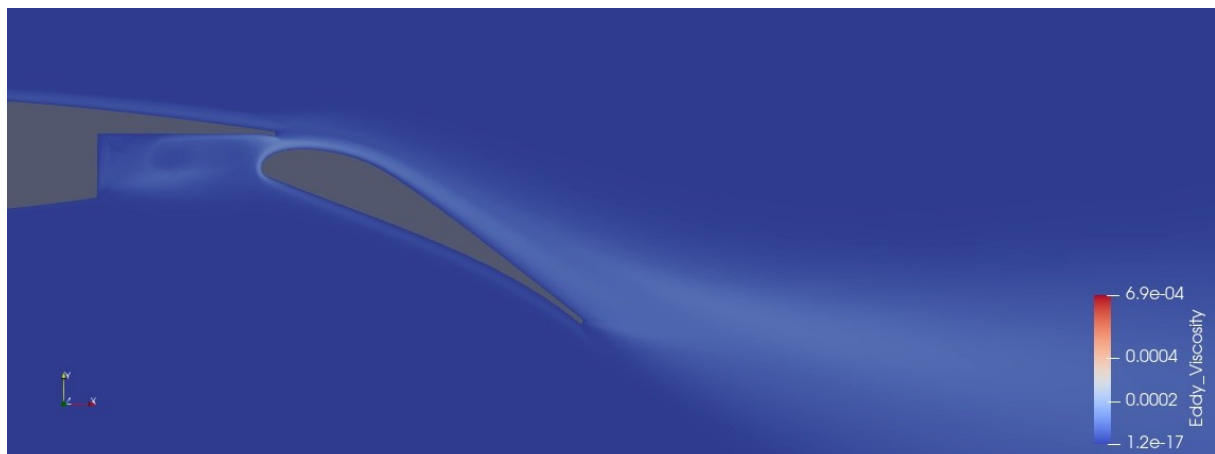


(a) Turbulent kinetic energy contours: Baseline configuration at 13-degree AoA and 30-degree flap deflection.

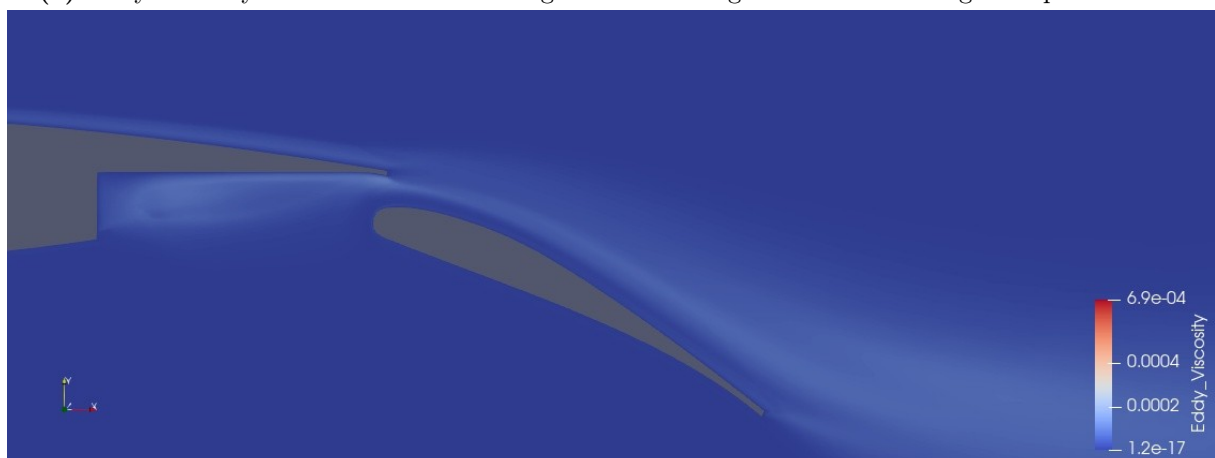


(b) Turbulent kinetic energy contours: Optimized configuration at 13-degree AoA and 30-degree flap deflection.

**Figure 4.9:** Turbulent kinetic energy contours: Comparison of baseline and optimized configurations at 13-degree AoA and 30-degree flap deflection.

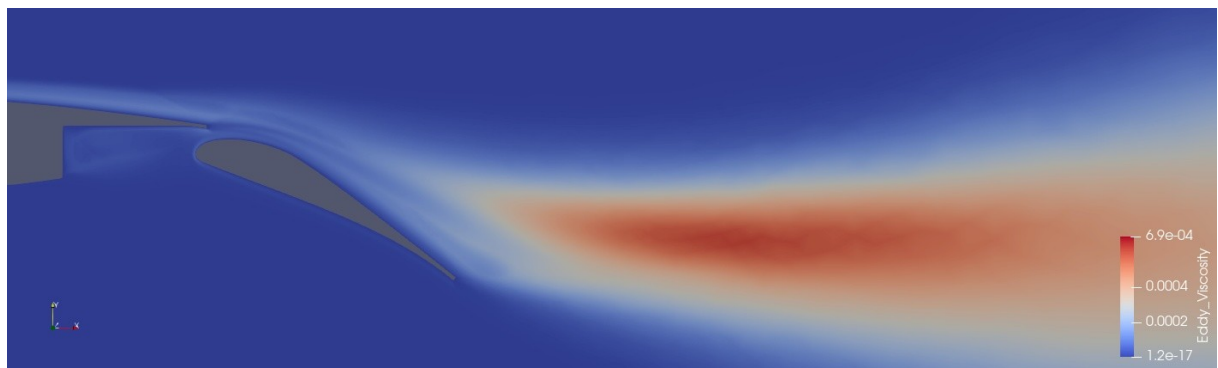


(a) Eddy viscosity contours: Baseline configuration at 4-degree AoA and 30-degree flap deflection.

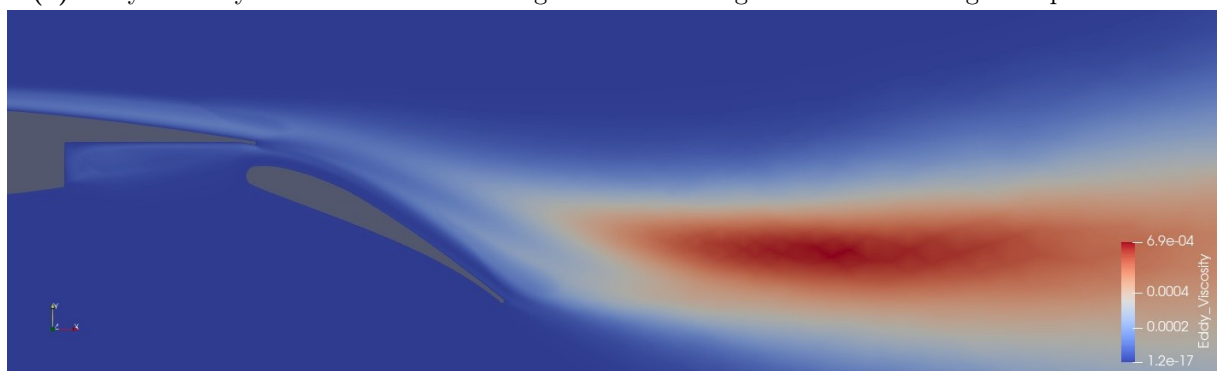


(b) Eddy viscosity contours: Optimized configuration at 4-degree AoA and 30-degree flap deflection.

**Figure 4.10:** Eddy viscosity contours: Comparison of baseline and optimized configurations at 4-degree AoA and 30-degree flap deflection.



(a) Eddy viscosity contours: Baseline configuration at 13-degree AoA and 30-degree flap deflection.



(b) Eddy viscosity contours: Optimized configuration at 13-degree AoA and 30-degree flap deflection.

**Figure 4.11:** Eddy viscosity contours: Comparison of baseline and optimized configurations at 13-degree AoA and 30-degree flap deflection.

## 4.4 Limitations and future work

- **Solver Framework Limitations (PyAeroSweep & SU2)**

The aerodynamic analysis conducted using PyAeroSweep and SU2 was limited to Reynolds-Averaged Navier-Stokes (RANS) simulations, specifically steady RANS. While RANS models offer computational efficiency, they average out unsteady flow structure, particularly in steady RANS, which may lead to not capturing the complexities of turbulent flows, particularly in separated regions and wakes, with the same accuracy as other higher-order methods. This limitation affects the accuracy of the predicted flow details, the magnitude of the aerodynamic coefficients as well as precise prediction of drag and stall characteristics.

To extend the capability of the current analysis, future studies could explore the use of Unsteady Reynolds-Averaged Navier-Stokes (URANS) simulations to capture time-dependent flow properties better and potentially improve the accuracy in regions of separated flows.

- **PyAeroSweep Workflow Instability**

The automated workflow using PyAeroSweep occasionally encountered errors (as illustrated in Figure 4.12). While the exact cause was not always determined, potential factors included issues with the warm start or inconsistencies with the convergence criteria due to the case converging too soon, leading to an incomplete output file. This led to active manual supervision, frequent intervention, and rerunning of multiple cases, which added to the total time and effort required.

Further development and debugging of PyAeroSweep scripts could improve the robustness and stability of the workflow, reducing frequent manual supervision and intervention.

```
Traceback (most recent call last):
  File "PyAeroSweep-main/Test_Cases/Flapped_airfoil_full/Input_data_flapped PARSEC.py", line
    214, in <module>
      run aerodynamic analysis (Input)
  File "PyAeroSweep-main/Run aerodynamic analysis.py", line 150, in run_aerodynamic_analysis
    run SU2.solve (Solver, Freestream, Mesh, Geometry)
  File "PyAeroSweep-main/Methods/Solver/run_SU2.py", line 98, in solve
    C1[i,j,k],Cd[i,j,k],Cm[i,j,k] = read_results('SU2_output.log')
  File "PyAeroSweep-main/Methods/Solver/run_SU2.py", line 315, in read_results
    C1= float(results_array[-4])
IndexError: list index out of range
```

**Figure 4.12:** PyAeroSweep error: Terminal output.

- **Mesh Quality, Refinement and System Limitation**

While mesh convergence studies were performed to ensure the reliability of the results for the chosen mesh settings, the equiangle skewness map (as shown in Figure 4.13) indicated areas where further mesh refinement could potentially improve the resolution of the flow, especially in the flap cutout, shroud tip and near the flap

leading edge. However, all the simulations were executed on a Linux workstation equipped with Intel® Core™ i7-10700K processor (8 cores, 16 threads @ 3.80 GHz) and 32 GB RAM. While sufficient for the full parameter sweep with the baseline mesh, the computational time was substantial.

Access to high-performance computing clusters would enable investigations with finer meshes and reduced run times, enabling a more extensive exploration of the design space.

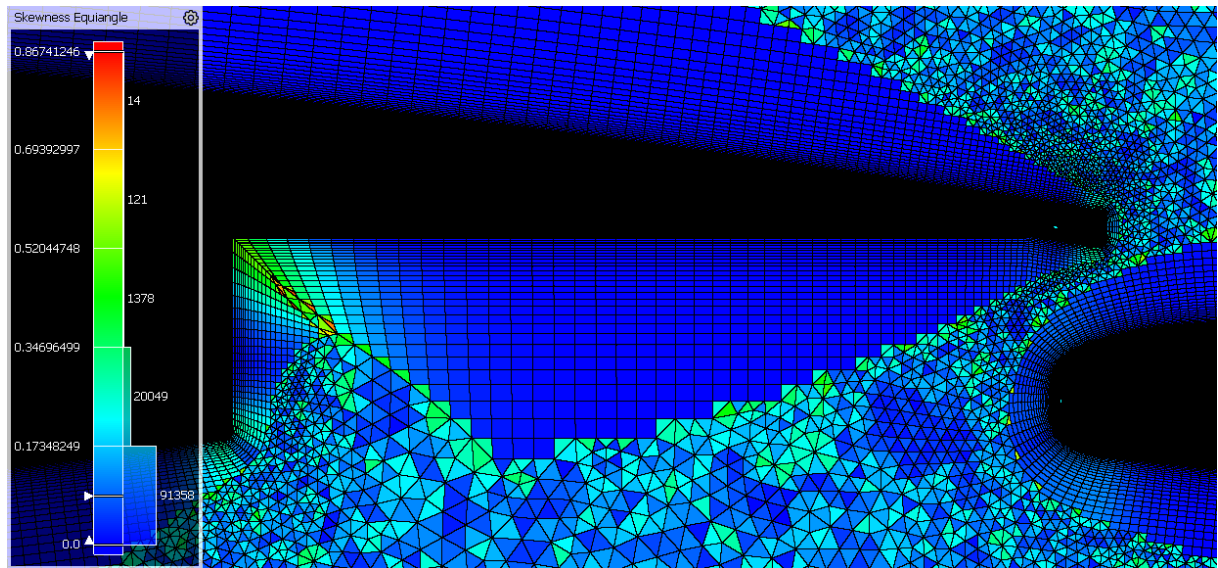


**Figure 4.13:** Equiangle skewness distribution of the baseline computational mesh.

- **Exhaustive Parameter Study and Manual Workflow Effort**

One of the most significant limitations of this study was the manual and highly time-consuming nature of the parametric analysis and optimization process. The parameter variation, extracting aerodynamic coefficient data, and post-processing had to be carried out semi-manually. In total, around 700 distinct CFD cases were systematically run as part of the whole thesis for both the 15-degree and 30-degree flap deflection angles.

However, the total number of cases including reruns due to failed simulations, manual testing of intermediate configurations, reruns due to lack of convergence and post-processing fixes, the actual number of simulations executed is well over 1000 individual CFD runs.

The `arrays.xlsx` file (Figure 2.3), intended to store the final  $C_L$ ,  $C_D$ , and  $C_M$  values for each sweep would be overwritten if a sweep was interrupted and restarted or if a new sweep with a different set of parameters was initiated. This resulted in a loss of data.

Also, a substantial effort was required to extract the aerodynamic coefficients from the individual case history files for each estimated 1000 simulation runs. This involved opening each case, extracting relevant data, and compiling it into an MS

Excel sheet, and generating plots - a highly time-consuming and labor-intensive process that impacted the overall efficiency of the study.

To enhance the efficiency of future studies, implementing a Multidisciplinary Design Optimization (MDO) concept such as Surrogate-Based Optimization (SBO) or using Automatic Optimization Algorithms could significantly reduce the number of simulations required and would also give a much better direction for parameter studies leading to better results.

### 4.5 Concluding remarks

This chapter documented the aerodynamic performance comparison between the baseline and the optimized Fowler flap configurations at 15-degree and 30-degree flap deflections. The primary objective was to maximize lift, a critical requirement for takeoff and landing.

The results demonstrated that the optimized design consistently achieved significantly higher maximum lift coefficients ( $C_{L_{max}}$ ) at both flap settings compared to the baseline, with an increase of 4.14% at 15-degree and 4.56% at 30-degree deflections respectively. Flow visualizations revealed that this improved lift was associated with enhanced flow control over the flap's upper surface and the leading edge.

While the optimized design exhibited a trade-off with potentially increased drag at higher lift coefficients and a less favorable lift-to-drag ratio in certain regimes, the significant gains in maximum lift achieved the primary objective of the design optimization study.

## 5 Summary

This thesis focused on the aerodynamic optimization of a Fowler flap for a Hybrid Laminar Flow Control (HLFC) airfoil, specifically aiming to maximize lift for the critical low-speed flight phases - takeoff (15-degree flap deflection) and landing (30-degree flap deflection). The work used the PyAeroSweep framework, which automates CFD analysis. This tool combines Fidelity Pointwise for generating high-quality grids around the aerodynamic surfaces and the SU2 solver for running steady RANS simulations with the  $k - \omega$  SST turbulence model.

The initial steps in the research involved a mesh sensitivity analysis, which ensured that the chosen mesh provided a good balance between accuracy and computational efficiency. This helped in establishing the reliability of the results, without unnecessary computational expense.

The core of the study involved a detailed parameter sensitivity analysis. The aim was to evaluate how different design parameters, such as the gap distances, flap chord ratio, and flap geometric curves affected the aerodynamic coefficients, specifically the lift coefficient ( $C_L$ ). This analysis included running simulations for different design configurations, totaling up to 1000 CFD runs. Even though the process was manually intensive, it was crucial for gaining a deep understanding of the influence of each parameter on lift performance.

From this extensive study, an optimized flap design was developed that significantly improved the maximum lift coefficient ( $C_{L_{\max}}$ ), as summarized in Table 5.1. For 15-degree flap deflection, the optimized design showed a 4.14% increase in maximum lift, while for 30-degree flap deflection, the increase was 4.56%. Flow visualizations were used to understand the influence of the change in design parameters on the improvement in performance. The optimized design exhibited enhanced flow control over the flap's surface and reduced flow instabilities within the channel flow, observed consistently across the range of angle of attack.

**Table 5.1:** Summary of maximum lift coefficient ( $C_{L_{\max}}$ ) improvements.

Flap Deflection	Baseline $C_{L_{\max}}$	Optimized $C_{L_{\max}}$	Percentage Improvement
15 degrees	2.90	3.02	4.14%
30 degrees	3.29	3.44	4.56%

Despite the limitations of steady RANS simulations and the need for manual data handling, the study successfully met its primary goal of maximizing lift for crucial flight phases. The approach, including the mesh and parameter studies, as well as flow visualization, provided valuable insights into optimizing high-lift devices for HLFC airfoils. This work lays a solid foundation for further research in high-lift system design, with the potential for incorporating more advanced techniques and automation in the future.

## Bibliography

- [1] European Commission, Commission, Directorate-General for Mobility, Transport, Directorate-General for Research and Innovation. *Flightpath 2050 – Europe’s vision for aviation – Maintaining global leadership and serving society’s needs*. Publications Office, 2011. DOI: doi/10.2777/50266.
- [2] ICAO. *Carbon Offsetting and Reduction Scheme for International Aviation (CORSIA)*. URL: <https://www.icao.int/environmental-protection/CORSIA/Pages/default.aspx>.
- [3] Airbus. *Winglets: a tip-top solution for more efficient aircraft*. URL: <https://www.airbus.com/en/newsroom/news/2017-02-winglets-a-tip-top-solution-for-more-efficient-aircraft> (visited on 25/03/2025).
- [4] Heinz Hansen. ‘Laminar Flow Technology - The Airbus View’. In: *27th International Congress of the Aeronautical Sciences*. Optimimage. 2010, pp. 2010–1.
- [5] Airbus. *ZEROe: our hydrogen-powered aircraft*. URL: <https://www.airbus.com/en/innovation/energy-transition/hydrogen/zeroe-our-hydrogen-powered-aircraft> (visited on 25/03/2025).
- [6] Advisory Council for Aviation Research and Innovation in Europe. *Time for change: Rethinking FlightPath 2050*. URL: [https://www.acare4europe.org/wp-content/uploads/2024/04/Time\\_for\\_change\\_FlightPath\\_2050-7.pdf](https://www.acare4europe.org/wp-content/uploads/2024/04/Time_for_change_FlightPath_2050-7.pdf) (visited on 25/03/2025).
- [7] S.N.V. Neigapula, S.P. Maddula and V.B. Nukala. ‘A study of high lift aerodynamic devices on commercial aircrafts’. In: *Aviation* 24.3 (2020), pp. 123–136. DOI: <https://doi.org/10.3846/aviation.2020.12815>.
- [8] Valerio Mosca, Anand Sudhi, Camli Badrya and Ali Elham. ‘Multidisciplinary Design Optimization of Transonic Wings with Boundary-Layer Suction’. In: *Journal of Aircraft* 61.2 (2024), pp. 523–542. DOI: <https://doi.org/10.2514/1.C037362>.
- [9] John Anderson. *EBOOK: Fundamentals of Aerodynamics (SI units)*. McGraw hill, 2011.
- [10] Daniel Raymer. *Aircraft design: a conceptual approach*. American Institute of Aeronautics and Astronautics, Inc., 2012.
- [11] Edward Lewis Houghton and Peter William Carpenter. *Aerodynamics for engineering students*. Elsevier, 2003.
- [12] Jochen Wild. *High-lift aerodynamics*. CRC Press, 2022.
- [13] Barnes W McCormick. *Aerodynamics, aeronautics, and flight mechanics*. John Wiley & Sons, 1994.
- [14] Joseph Katz and Allen Plotkin. *Low-speed aerodynamics*. Vol. 13. Cambridge university press, 2001.
- [15] Nils Beck, Tim Landa, Arne Seitz, Loek Boermans, Yaolong Liu and Rolf Radespiel. ‘Drag reduction by laminar flow control’. In: *Energies* 11.1 (2018), p. 252.

## Bibliography

---

- [16] Antonio Filippone. *Advanced aircraft flight performance*. Vol. 34. Cambridge University Press, 2012.
- [17] Daniel Reckzeh. ‘Multifunctional wing moveables: design of the A350XWB and the way to future concepts’. In: *29th congress of the international council of the aeronautical sciences*. International Council of Aeronautical Sciences (ICAS) St. Petersburg. 2014.
- [18] Henning Strüber. ‘The aerodynamic design of the A350 XWB-900 high lift system’. In: *29th international congress of the aeronautical sciences*. International Council of the Aeronautical Sciences. 2014.
- [19] PT Meredith. ‘Viscous phenomena affecting high-life systems and suggestions for future CFD development’. In: *High-Lift System Aerodynamics* (1993).
- [20] Sustainable and Energy-Efficient Aviation (SE<sup>2</sup>A). *Sustainable and Energy-Efficient Aviation (SE<sup>2</sup>A)*. visited on (26.03.2025). 2025. URL: <https://www.tu-braunschweig.de/en/se2a>.
- [21] Mauro Minervino, Pierluigi Iannelli and D. Quagliarella. ‘3D Flap Design using Navier-Stokes Equations and Evolutionary Optimization Techniques on an Industrial Platform’. In: Sept. 2011. DOI: [10.13140/2.1.2211.0083](https://doi.org/10.13140/2.1.2211.0083).
- [22] Frank M White. ‘Fluid Mechanics, McGraw-Hill’. In: *New York* (1994).
- [23] Florian R Menter. ‘Two-equation eddy-viscosity turbulence models for engineering applications’. In: *AIAA journal* 32.8 (1994), pp. 1598–1605.
- [24] NASA - Langley Research Center. *The Menter Shear Stress Transport Turbulence Model*. URL: <https://turbmodels.larc.nasa.gov/sst.html> (visited on 07/04/2025).
- [25] Mohammad H Sadraey. *Aircraft design: A systems engineering approach*. John Wiley & Sons, 2024.
- [26] D. N. Foster, Hamlyn Peter Anthony Hugh Irwin and B. R. Williams. ‘The two-dimensional flow around a slotted flap’. In: *Aeronautical Research Council, Reports and Memoranda* (1970), p. 3681.
- [27] Snorri Gudmundsson. *General aviation aircraft design: Applied Methods and Procedures*. Butterworth-Heinemann, 2013.
- [28] Egbert Torenbeek. *Synthesis of subsonic airplane design: an introduction to the preliminary design of subsonic general aviation and transport aircraft, with emphasis on layout, aerodynamic design, propulsion and performance*. Springer Science & Business Media, 2013.

# Appendix

## A Input\_data.py for the case Flapped\_airfoil\_full

```

1 import numpy as np
2 from Core.Data import Data
3 from Components.Solver import Solver
4 from Components.Geometry import Geometry
5 from Components.Geometry.Wing.Segment import Segment
6 from Components.Mesh import Mesh
7
8 from Run_aerodynamic_analysis import run_aerodynamic_analysis
9
10 def Input_data():
11
12     working_dir = r"path/to/the/working/directory"
13
14 # -----SOLVER SETTINGS----- #
15
16     Solver_settings = Solver()
17
18     Solver_settings.working_dir = working_dir
19
20     Solver_settings.name = 'SU2' # SU2 or Fluent
21
22     # Solver dimensions
23     # 2d or 3d for SU2
24     Solver_settings.dimensions = '2d'
25
26     # Only available for SU2 in 3D
27     # Defines half of the shape or a full shape analysis (Only symmetric works for now)
28     Solver_settings.symmetric = True
29
30     # SST or SA for SU2
31     Solver_settings.turbulence_model = 'SST'
32
33     # Number of processors
34     Solver_settings.processors = 7
35
36     # Cauchy convergence criteria
37     # Could be either LIFT or DRAG
38     Solver_settings.monitor = "LIFT"
39     Solver_settings.tolerance = 5e-7
40     Solver_settings.max_iterations = 25000
41     Solver_settings.save_frequency = 500
42
43     # Warm start
44     # YES or NO
45     Solver_settings.warmstart = 'YES'
46
47     # SU2 reference config file name which will be updated
48     Solver_settings.config_file = 'Run_airfoil_template.cfg'
49

```

---

## Appendix

```
50
51
52 # -----FREESTREAM SETTINGS----- #
53
54
55 Freestream = Data()
56 Freestream.Mach          = np.array([0.21])
57 Freestream.Altitude      = np.array([0]) # in meters
58 Freestream.Angle_of_attack = np.array([0]) # in degrees (0,2,4,...10,11,...20)
59
60
61
62 # -----GEOMETRY SETTINGS----- #
63
64
65
66 Geometry_data = Geometry()
67
68 # Geometry to analyze
69 ''' Could be airfoil or wing
70     Airfoils can be parametrically defined using the PARSEC methods
71     Wings are defined only using the existing CAD file and work either for
72     straight tapered wings with or without the kink'''
73
74 Geometry_data.type = 'airfoil'
75
76 # Reference values
77 Geometry_data.reference_values = {
78     "Area"   : 3.28,
79     "Length" : 3.28,
80     "Depth"  : 1,
81     "Point"  : [0.25*3.28,0,0]      # reference point about which the moment is taken
82 }
83
84 # Flag to use PARSEC parametrization or to use already existing airfoils
85 Geometry_data.generate = True
86
87 segment = Segment()
88 segment.tag           = 'section_1'
89 segment.chord          = 3.28
90 segment.Airfoil.files = {
91     "upper" : "main_airfoil_upper_1.dat",
92     "lower" : "main_airfoil_lower_1.dat"
93 }
94 segment.Airfoil.PARSEC = {
95     "rle"       : 0.0073,
96     # Main airfoil LE radius
97     "x_pre"    : 0.487562059408678,
98     # x-location of the crest on the pressure side
99     "y_pre"    : -0.043736966713945,
100    # y-location of the crest on the pressure side
101    "d2ydx2_pre": 0.631519657420421,
102    # curvature of the crest on the pressure side
```

---

## Appendix

```
99          "th_pre"      : -10.0,
100         # trailing edge angle on the pressure side [deg]
101         "x_suc"       : 0.441822291030641,
102         # x-location of the crest on the suction side
103         "y_suc"       : 0.060104062855903,
104         # y-location of the crest on the suction side
105         "d2ydx2_suc": -0.423082569160247,
106         # curvature of the crest on the suction side
107         "th_suc"      : -10.691704859160257,
108         # trailing edge angle on the suction side [deg]
109         "yte_upper"   : 0.002,
110         "yte_lower"   : -0.002
111     }
112
113     segment.TrailingEdgeDevice.type = 'Slotted'
114     segment.TrailingEdgeDevice.PARSEC = {
115         "cf_c"        : 0.3,      # flap chord ratio
116         "ce_c"        : 0.375,    # conical curve extent ratio wrt the flap chord length
117         "csr_c"        : 0.9,      # shroud chord ratio
118         "clip_ext"    : 0.05,    # shroud lip extent ratio wrt the flap
119         "r_le_flap"   : 0.0135,   # flap leading edge radius
120         "tc_shr_tip" : 0.003,    # shroud tip thickness
121         "w_conic"     : 0.75,    # conical parameter for the suction side of the flap airfoil
122         "delta_f"     : 15/30,
123         # flap deflection [deg] [15 Deg - Take Off, 30 Deg - Landing]
124         "x_gap"       : 0.0075,
125         # x-length gap from the shroud TE (positive value is moving the flap left)
126         "y_gap"       : 0.0197,
127         # y-length gap from the shroud TE (positive value is moving the flap down)
128     }
129
130     segment.TrailingEdgeDevice.files = {
131         "upper surface file" : "flap_airfoil_upper.dat",
132         "lower surface file" : "flap_airfoil_lower.dat",
133         "flap cutout"       : ["main_airfoil_cut1.dat", "main_airfoil_cut2.dat"]
134     }
135
136     segment.LeadingEdgeDevice.type = 'Droop'
137     segment.LeadingEdgeDevice.PARSEC = {
138         "delta_s"       : 25,      # droop nose deflection [deg]
139         "cs_c"         : 0.13,    # droop nose chord ratio
140         "d_cs_up"      : 0.03,    # droop nose offset from the hinge on the upper surface
141         "d_cs_low"     : 0.03,    # shroud lip extent ratio wrt the flap
142         "w_con_seal"   : 1.0,     # conical parameter for the droop nose seal
143     }
144
145     segment.plot_airfoil = True
146
147     Geometry_data.Segments.append(segment)
```

```

148
149 # -----MESH SETTINGS----- #
150
151 Mesh_data = Mesh()
152
153 # Flag to mesh the shape or not
154 Mesh_data.meshing      = True
155
156 # Mesh type
157 Mesh_data.structured = False
158
159 # Defined the OS in which Pointwise is used
160 # WINDOWS or Linux
161 Mesh_data.operating_system = 'Linux'
162
163 # Pointwise tclsh directory used in Windows
164 Mesh_data.tclsh_directory = r"path/to/the/tclsh/directory"
165
166 # Desired Y+ value
167 Mesh_data.Yplus = 1.0
168
169 # Define the Glyph template to use for meshing
170 Mesh_data.glyph_file = "mesh_flapped_airfoil_SU2.glf"
171
172 # Mesh filename for either the newly generated mesh or an existing mesh
173 Mesh_data.filename = 'su2meshEx.su2'
174
175 # Define far-field
176 #   min x, max x
177 #   min y, max y
178 #   min z, max z (used only for 3D cases)
179 Mesh_data.far_field = [[-60, 60], [-60, 60]]
180
181
182 Mesh_data.airfoil_mesh_settings = {
183     "LE_spacing"           : 0.001,  # Airfoil leading edge spacing
184     "TE_spacing"           : 0.0005, # Airfoil trailing edge spacing
185     "LE_flap_spacing"      : 0.001,
186     "TE_flap_spacing"      : 0.0005,
187     "flap_cut_cluster"     : 0.005,  # Cluster at the flap cutout corner
188     "connector dimensions" : [200, 120, 150, 150, 70, 25, 8, 8],
189     "near-field refinement radius 1" : 9,
190     "near-field refinement radius 2" : 45,
191     "near-field nodes"       : 100,
192     "far-field connectors"  : 20,
193     "Max TREX layers"      : 100,
194     "near-field boundary decay 0" : 0.85,
195     "Full TREX layers"     : 60,
196     "TREX growth rate"     : 1.15,
197     "near-field boundary decay 2" : 0.85,
198     "near-field boundary decay 1" : 0.85
199 }
200
201

```

```
202 # ----- #
203
204     # Pack all inputs
205     Input = Data()
206     Input.Solver          = Solver_settings
207     Input.Freestream       = Freestream
208     Input.Geometry        = Geometry_data
209     Input.Mesh            = Mesh_data
210
211
212     return Input
213
214
215 if __name__ == '__main__':
216
217     Input = Input_data()
218     run_aerodynamic_analysis(Input)
219
220 #Connector Dimensions
221 # [200, 120, 150, 150, 70, 25, 8, 8],   Baseline
222 # [260, 156, 195, 195, 91, 32, 8, 8],   Fine    (30%+)
223 # [140, 84, 105, 105, 49, 17, 8, 8],   Coarse  (30%-)
```

**Listing 1:** Content of Input\_data\_flapped\_PARSEC.py for the case Flapped\_airfoil\_full.

## B Geometric input data for the HLFC airfoil: PARSEC & CST

```

1 segment.Airfoil.PARSEC = {
2     "rle"      : 0.0073,
3                     # main airfoil LE radius
4     "x_pre"    : 0.487562059408678,
5                     # x-location of the crest on the pressure side
6     "y_pre"    : -0.043736966713945,
7                     # y-location of the crest on the pressure side
8     "d2ydx2_pre": 0.631519657420421,
9                     # curvature of the crest on the pressure side
10    "th_pre"   : -10.0,
11                     # trailing edge angle on the pressure side [deg]
12    "x_suc"    : 0.441822291030641,
13                     # x-location of the crest on the suction side
14    "y_suc"    : 0.060104062855903,
15                     # y-location of the crest on the suction side
16    "d2ydx2_suc": -0.423082569160247,
17                     # curvature of the crest on the suction side
18    "th_suc"   : -10.691704859160257,
19                     # trailing edge angle on the suction side [deg]
20    "yte upper": 0.002,
21                     #y-coordinate on the upper trailing edge
22    "yte lower": -0.002
23                     #y-coordinate on the lower trailing edge      }
24

```

**Listing 2:** Airfoil definition - PARSEC

```

1 segment.Airfoil.CST = {
2     "upper"    : [ 0.20095, 0.26864, 0.10933, 0.29307,\n
3                     0.12099, 0.21197, 0.18002, 0.18408],\n
4                     #shape coefficients for upper surface
5     "lower"    : [-0.20095, 0.05433, -0.46373, 0.25546,\n
6                     -0.40375, 0.01032, -0.14109, -0.11217],\n
7                     #shape coefficients for lower surface
8     "N1 upper": 0.5,\n
9                     #leading edge shape - upper
10    "N1 lower": 0.5,\n
11                     #leading edge shape - lower
12    "N2 upper": 1.0,\n
13                     #trailing edge shape - upper
14    "N2 lower": 1.0,\n
15                     #trailing edge shape - Lower
16    "yte upper": 0.001,
17                     #y-coordinate on the upper trailing edge
18    "yte lower": -0.001
19                     #y-coordinate on the lower trailing edge      }
20

```

**Listing 3:** Airfoil definition - CST

## C SU2: Solver configuration file

```

1 % ----- SOLVER -----
2 %
3 SOLVER= RANS
4 KIND_TURB_MODEL= SST
5 REF_DIMENSIONALIZATION= FREESTREAM_VEL_EQ_MACH
6 %
7 % ----- FREESTREAM -----
8 %
9 MACH_NUMBER= 0.21
10 AOA= 2
11 INIT_OPTION= REYNOLDS
12 FREESTREAM_OPTION= TEMPERATURE_FS
13 FREESTREAM_TEMPERATURE= 288.16
14 REYNOLDS_NUMBER= 16047713
15 REYNOLDS_LENGTH= 3.28
16 %
17 % ----- REFERENCE VALUES -----
18 %
19 REF_AREA= 3.28
20 REF_LENGTH= 3.28
21 REF_ORIGIN_MOMENT_X= 0
22 REF_ORIGIN_MOMENT_Y= 0.0
23 REF_ORIGIN_MOMENT_Z= 0.0
24 %
25 % ----- BOUNDARY CONDITIONS -----
26 %
27 MARKER_HEATFLUX= ( wall, 0.0 )
28 MARKER_FAR= ( far-field )
29 MARKER_PLOTTING= ( wall )
30 MARKER_MONITORING= ( wall )
31 %
32 % ----- FLUID MODELS -----
33 %
34 FLUID_MODEL= STANDARD_AIR
35 GAMMA_VALUE= 1.4
36 GAS_CONSTANT= 287.058
37 %
38 VISCOSITY_MODEL= SUTHERLAND
39 MU_REF= 1.716E-5
40 MU_T_REF= 273.15
41 SUTHERLAND_CONSTANT= 110.4
42 %
43 CONDUCTIVITY_MODEL= CONSTANT_PRANDTL
44 PRANDTL_LAM= 0.72
45 PRANDTL_TURB= 0.90
46 %
47 % ----- SPATIAL DISCRETIZATION -----
48 %
49 NUM_METHOD_GRAD= GREEN_GAUSS
50 CONV_NUM_METHOD_FLOW= ROE
51 ENTROPY_FIX_COEFF= 1e-5
52 MUSCL_FLOW= YES

```

---

## Appendix

---

```
53 SLOPE_LIMITER_FLOW= VAN_ALBADA_EDGE
54 %
55 CONV_NUM_METHOD_TURB= SCALAR_UPWIND
56 MUSCL_TURB= NO
57 %
58 % ----- PSEUDOTIME INTEGRATION / CONVERGENCE ACCELERATION -----
59 %
60 USE_VECTORIZATION= YES
61 TIME_DISCRE_FLOW= EULER_IMPLICIT
62 TIME_DISCRE_TURB= EULER_IMPLICIT
63 %
64 CFL_NUMBER= 25
65 CFL_REDUCTION_TURB= 1.0
66 CFL_ADAPT= YES
67 CFL_ADAPT_PARAM= ( 0.1, 1.2, 25.0, 1e3 )
68 %
69 %
70 LINEAR_SOLVER= FGMRES
71 LINEAR_SOLVER_PREC= ILU
72 LINEAR_SOLVER_ERROR= 0.2
73 LINEAR_SOLVER_ITER= 4
74 %
75 MGLEVEL= 0
76 NEWTON_KRYLOV= YES
77 NEWTON_KRYLOV_IPARAM= ( 0, 0, 1 ) % n0, np, ft
78 NEWTON_KRYLOV_DPARAM= ( 0.0, 1e-20, -3, 1e-5 ) % r0, tp, rf, e
79 %
80 % ----- CONVERGENCE CRITERIA -----
81 %
82 ITER= 25000
83 %
84 % Convergence criteria (CAUCHY, RESIDUAL)
85 CONV_FIELD= LIFT %CAUCHY
86 %
87 CONV_RESIDUAL_MINVAL= -11.5
88 %
89 % Start convergence criteria at iteration number
90 CONV_STARTITER= 10
91 %
92 % Number of elements to apply the criteria
93 CONV_CAUCHY_ELEMS= 500
94 %
95 % Epsilon to control the series convergence
96 CONV_CAUCHY_EPS= 5e-07
97 %
98 %
99 % ----- INPUT / OUTPUT -----
100 %
101 MESH_FILENAME= su2meshEx.su2
102 MESH_FORMAT= SU2
103 RESTART_SOL= YES
104 SOLUTION_FILENAME = solution_flow
105 OUTPUT_WRT_FREQ= 500
106 SCREEN_WRT_FREQ_INNER= 25
```

```
107 HISTORY_OUTPUT= ( ITER, RMS_RES, AERO_COEFF )
108 SCREEN_OUTPUT= ( INNER_ITER, RMS_DENSITY, RMS_MOMENTUM-X, RMS_MOMENTUM-Y,\n
109             RMS_ENERGY, RMS_NU_TILDE, DRAG, LIFT, MOMENT_Z,\n
110             LINSOL_RESIDUAL )
```

**Listing 4:** SU2: Configuration file